

TRACING RAM-PRESSURE STRIPPING WITH WARM MOLECULAR HYDROGEN EMISSION

SURESH SIVANANDAM^{1,2}, MARCIA J. RIEKE², AND GEORGE H. RIEKE²

Accepted by The Astrophysical Journal

ABSTRACT

We use the *Spitzer* Infrared Spectrograph (IRS) to study four infalling cluster galaxies with signatures of on-going ram-pressure stripping. H₂ emission is detected in all four; two show extraplanar H₂ emission. The emission usually has a warm (T ~ 115 – 160K) and a hot (T ~ 400 – 600K) component that is approximately two orders of magnitude less massive than the warm one. The warm component column densities are typically 10¹⁹ – 10²⁰ cm⁻² with masses of 10⁶ – 10⁸ M_⊙. The warm H₂ is anomalously bright compared with normal star-forming galaxies and therefore may be excited by ram-pressure. In the case of CGCG 97-073, the H₂ is offset from the majority of star formation along the direction of the galaxy’s motion in the cluster, suggesting it is forming in the ram-pressure wake of the galaxy. Another galaxy, NGC 4522, exhibits a warm H₂ tail approximately 4 kpc in length. These results support the hypothesis that H₂ within these galaxies is shock-heated from the interaction with the intracluster medium. Stripping of dust is also a common feature of the galaxies. For NGC 4522, where the distribution of dust at 8 μm is well resolved, knots and ripples demonstrate the turbulent nature of the stripping process. The Hα and 24 μm luminosities show that most of the galaxies have star formation rates comparable to similar mass counterparts in the field. Finally, we suggest a possible evolutionary sequence primarily related to the strength of ram-pressure a galaxy experiences to explain the varied results observed in our sample.

Subject headings: galaxies: clusters: intracluster medium — galaxies: evolution — galaxies: ISM — infrared: galaxies

1. INTRODUCTION

Ram-pressure stripping is thought to transform infalling galaxies in the cluster environment (Gunn & Gott 1972) and may explain the distinctly different properties of cluster galaxies when compared to the field. The traditional paradigm of stripping confined to just atomic gas is being challenged. Observations show that molecular gas can be stripped from a cluster galaxy and extend to well beyond the tidal radius of the galaxy (Sivanandam et al. 2010). Other observations show star forming trails emanating from infalling galaxies in clusters (Cortese et al. 2007; Sun et al. 2010; Sivanandam et al. 2010). While originally thought to be fairly rare (Sun et al. 2010), recent deep narrowband Hα and *GALEX* UV observations in the Coma cluster show at least a dozen galaxies with long (~ 20 – 100 kpc) Hα trails (Yagi et al. 2010) and UV trails (Smith et al. 2010) all generally pointing away from the cluster centre, indicating that ram-pressure can strip gas, and stars can form well beyond the gravitational well of the stripped galaxy.

The traditional view is that ram-pressure does not have sufficient strength to remove significant amounts of molecular gas from galaxies, based on the observation that cluster galaxies typically show little correlation between deficiencies in atomic (HI) and molecular gas (Boselli & Gavazzi 2006). The removal of just the HI gas, which in turn no longer replenishes the H₂ reservoir, will impact the star forming properties of galaxies only slowly, since the H₂ gas consumption time scale in nearby

disk galaxies is approximately 2 Gyr (Bigiel et al. 2011). The observations of stripped molecular gas suggest that the suppression process may operate more quickly. Other studies also suggest that the molecular component is affected by ram pressure, because there is a correlation between H₂ deficiency and galaxies that have lost HI within their optical disks (Fumagalli et al. 2009). Furthermore, Herschel observations of cluster galaxies reveal truncated disks, indicating erosion of their molecular components (Cortese et al. 2010; Corbelli et al. 2012). The rapid removal of molecular gas would have a relatively quick impact on the star-forming properties of galaxies. This possibility would agree with other studies (e.g., Poggianti et al. 1999; Bai et al. 2007) that infer relatively rapid quenching of star formation in clusters.

A more complete view is required to understand fully the role ram-pressure stripping plays in the evolution of a cluster galaxy. The discovery of a galaxy group scale shock in Stephan’s Quintet (Appleton et al. 2006; Cluver et al. 2010) glowing in ground-state rotational lines of warm molecular hydrogen (H₂) pointed toward a new method to detect ram-pressure stripped molecular hydrogen, and to study the shock associated with the interaction between the intracluster medium (ICM) and interstellar medium (ISM) of a galaxy experiencing ram-pressure stripping. Cluver et al. (2010) used *Spitzer*’s infrared spectrograph to generate a large-area spectral map of this shock; they find a large amount of H₂ (~ 5 × 10⁸ M_⊙) within the main shock region where ground-state rotational lines of warm H₂ are the main coolant. Unexpectedly, considerable CO emission, a tracer of cold H₂, was discovered within this shock (Guillard et al. 2012a), indicating that there is a significant cold gas reservoir in the intragroup medium. The

¹ Dunlap Fellow, Dunlap Institute for Astronomy and Astrophysics, University of Toronto, Rm 101, 50 St. George St, Toronto, ON, Canada M5S 3H4; sivanandam@di.utoronto.ca

² Steward Observatory, University of Arizona, 933 North Cherry Ave, Tucson, AZ, USA 85721

group-wide shock is thought to be produced by the collision of an intruder galaxy with the intragroup medium at a velocity of $\sim 1000 \text{ km s}^{-1}$ (Cluver et al. 2010). The collision velocity is similar to the relative velocity between the ISM of an infalling galaxy and the ICM of a dense cluster, which motivated our survey for similar features of shocked H_2 emission in candidate galaxies in nearby clusters. The H_2 emission may serve as a direct tracer of the removal of molecular gas in these galaxies, which may immediately impact the star forming properties of these systems.

We have searched for warm molecular hydrogen (H_2) emission from four galaxies that show strong signs of on-going ram-pressure stripping. ESO 137-001, an infalling spiral in the rich cluster Abell 3627, was the first galaxy observed by our program and was also the best candidate for detecting this emission, as it had spectacular X-ray and $\text{H}\alpha$ tails extending 70 and 40 kpc, respectively (Sun et al. 2007). Through *Spitzer* Infrared Spectrograph (IRS) imaging spectroscopy, we detected a striking warm H_2 tail ($T \sim 130\text{--}160\text{K}$) extending at least 20 kpc from this galaxy (Sivanandam et al. 2010, hereafter referred to as Paper 1). The H_2 tail was found to be co-aligned with the X-ray and $\text{H}\alpha$ tails, and extended farther than the tidal radius of the galaxy. The tail included most of the extraplanar star forming regions, which led to our conclusion that the H_2 being stripped from the galaxy fostered star formation. The most tantalizing discovery was that the warm H_2 emission was not powered by star formation, which is the most common excitation mechanism. Similar signatures of unusually strong warm H_2 emission have been detected in cool-core clusters in their central regions within their brightest cluster galaxies (Egami et al. 2006; Donahue et al. 2011) and along extended filaments (Johnstone et al. 2007). Within this cooling flow environment, multiple heating mechanisms for H_2 have been suggested including cosmic ray heating, conduction, and dissipative magnetohydrodynamic (MHD) waves Ferland et al. (2008, 2009). Other potential mechanisms have also been discussed such as X-ray dissociation regions (XDRs) (Maloney et al. 1996). Our previous work suggested that the H_2 is being dissociated by a shock produced by the interaction between the ICM and galactic interstellar medium and is reforming in the post-shock region in an excited state. Recently Wong et al. (2014) also detected similar enhanced H_2 emission, albeit at a lower level, in four ram-pressure stripped Virgo galaxies and they also favour shock excitation as the explanation for the anomalous H_2 emission. However, these alternative heating mechanisms have not been definitely ruled out.

We explore these possibilities further in our expanded sample of three more galaxies that have clear signs of on-going ram-pressure stripping. CGCG 97-073 (hereafter referred to as 97073) is an irregular galaxy with a 50 kpc long $\text{H}\alpha$ tail (Gavazzi et al. 2001) in another rich cluster, Abell 1367. NGC 4522 is a type SBcd spiral in the Virgo cluster with arc shaped $\text{H}\alpha$ emission and with prominent extraplanar star formation, a truncated $\text{H}\alpha$ disk (Kenney & Koopmann 1999), and a truncated and displaced HI distribution (Kenney et al. 2004). Finally, NGC1427A is a dwarf irregular galaxy in the Fornax cluster with prominent arc-shaped morphology and star formation along one edge (Georgiev et al. 2006), which

is likely explained by the interaction with the Fornax’s ICM (Chanamé et al. 2000). Our detecting and characterizing warm H_2 and extended emission by dust from these galaxies provides a more complete picture of how common molecular gas stripping is in different cluster environments, and how ram-pressure impacts infalling galaxies.

The paper is organized as follows. In Section 2, we present the sources of our data and the methodology used to analyze the imaging and spectroscopic data. In Section 3, we present the results from our data reduction, and characterize the properties of the warm H_2 and dust and determine the star-forming properties of the galaxies. In Section 4, we place the star formation rates of the sample galaxies in a broader context and discuss the possible excitation mechanisms for H_2 , including how effectively excess warm H_2 may trace ram-pressure stripping. We also provide a possible explanation for the variety of results among these galaxies. Finally in Section 5, we list our conclusions. For computing distances, we adopt the concordance cosmological model ($\Omega_\Lambda = 0.73$, $\Omega_m = 0.27$, and $H_0 = 71 \text{ km s}^{-1} \text{ Mpc}^{-1}$). All reported errors in this work are quoted at the 1σ level.

2. OBSERVATIONS AND DATA REDUCTION

To detect and characterize the warm molecular hydrogen in our sample of galaxies, we carried out a *Spitzer* GTO program 50213 (PI: G. Rieke), in which we spectrally mapped the galaxies with *Spitzer*’s infrared spectrograph (IRS) and imaged the galaxies with the infrared array camera (IRAC). We also compiled an ancillary dataset consisting of archival *Hubble*, GOLDMine (Gavazzi et al. 2003), and *Spitzer* data. This heterogeneous dataset consists of optical-band *HST* images, $\text{H}\alpha$ images, additional *Spitzer* IRAC images, and additional IRS spectral mapping data.

2.1. IRAC Imaging

We obtained data for each galaxy in all four (3.6, 4.5, 5.7, and $8 \mu\text{m}$) IRAC channels (Fazio et al. 2004). IRAC imaging of 97073 and NGC 1427A was carried out as part of our *Spitzer* GTO program. IRAC data for NGC 4522 were obtained from the *Spitzer* Science Archive, observed as part of program 30945 (PI: J. Kenney). We constructed IRAC mosaics of the galaxy with MOPEX (version 18.3.1) using the Basic Calibrated Data (BCD) from the *Spitzer* pipeline (version S18.7) as input and following the *Spitzer* Science Center (SSC) IRAC reduction cookbook. To reduce banding artifacts, corrected BCDs were used as input for the construction of $8 \mu\text{m}$ mosaics. Bad pixel rejection was achieved through dithering, median filtering, and masking of known bad pixels using pixel masks provided by the SSC.

We also construct $8 \mu\text{m}$ excess images for each galaxy to study its star-forming properties using the same method outlined in Paper 1. Excess $8 \mu\text{m}$ flux in galaxies is often produced by warm dust rich in aromatic hydrocarbons, which is associated with star formation regions (Calzetti et al. 2007). Our technique subtracts the stellar continuum from the $8 \mu\text{m}$ image by subtracting a resolution-matched, flux-scaled, and well-registered $3.6 \mu\text{m}$ image. We verify the effectiveness of our method by ensuring the foreground stars in our field are adequately subtracted in the final $8 \mu\text{m}$ excess image.

2.2. *HST* Imaging

We obtained *HST* Advanced Camera for Surveys (ACS) archival data for NGC 1427A (Proposal ID: 9689; PI: M. Gregg) and NGC 4522 (Proposal ID: 9773; PI: J. Kenney). We used the F660N (narrowband H α) and F775W (SDSS I-band) data for NGC 1427A and F435W (B-band) and F814 (I-band) data for NGC 4522. We obtained the pipeline-reduced multidrizzled data for our analysis. To construct the H α image for NGC 1427A, we used the F660N and F775W filter data. The pipeline reduced data for each filter were already properly registered as part of the pipeline processing. We simply scaled the F775W data and subtracted it from the F660N data to remove the stellar contribution from the narrowband image. We verified the success of our subtraction by ensuring the foreground stars in the field were adequately subtracted. Due to the poor signal-to-noise of the subtracted data, we binned and smoothed the data to improve the visibility of H α emitting regions. Because of the finite width of the narrowband filter, there will be some contamination from [NII] lines that are close to the H α wavelength.

2.3. *IRS* Spectral Mapping

Our IRS observations used both the short-low (SL) and long-low (LL) IRS modules that together span 5.3 to 38.0 μm (Houck et al. 2004). The complete wavelength range allows us to observe several ground vibrational state H₂ rotational lines, specifically the $\nu=0-0$ S(0) thru S(7) transitions, that can be used to characterize the thermodynamic properties of warm H₂. The spectral mapping techniques and data analysis methods are discussed in Paper 1. We use the most recent IRS pipeline-reduced BCD files (version S18.7) and *CUBISM* (version 1.7; Smith et al. 2007) to construct our spectral cubes. Bad pixels are eliminated visually using the same method described in Paper 1, and the initial background subtraction is carried out by subtracting the background measured with the outrigger pointings. However, additional background subtraction was required for some observations because the outrigger pointing background subtraction did not remove all of the flux due to background gradients. In these cases, we generated a background spectrum for each spectral map by averaging the spectra in source-free regions. This background was then subtracted, and the error of the background spectrum was included in the final spectral map flux uncertainties. For the case of NGC 4522, we supplement our analyses with archival LL spectrograph data from another *Spitzer* program (Proposal ID: 50819; PI: J. Kenney). We use the same methods of background subtraction and bad pixel rejection for analyzing the archival dataset. The coverage maps for the two different sets of observations for NGC 4522 are quite different. Our IRS observations cover the entire galaxy, but the archival observations are deeper and focus on two specific locations where ram-pressure is thought to be stripping significant amounts of gas. The archival observations have approximately two to three times more integration time per sky pixel than our observations (~ 90 s versus 250 s for LL2 and 150 s versus 250 s for LL1) and use a similar mapping strategy. The IRS coverage maps for 97073, NGC 4522, and NGC 1427A are shown in Figures 1, 2, and 3. The cov-

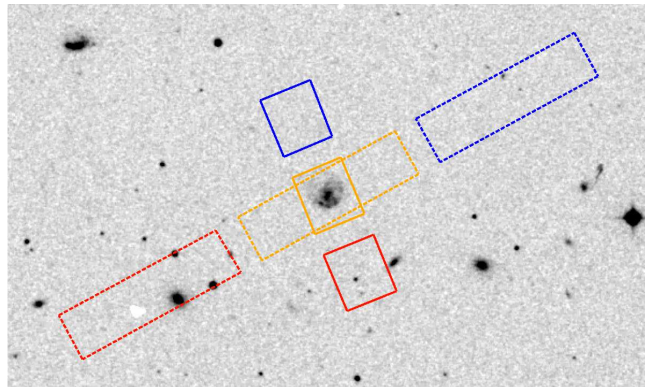


FIG. 1.— $6' \times 10'$ map digitized sky survey (DSS) image of CGCG 97-073 with *Spitzer* IRS pointings overlaid. The solid and dashed boxes represent the short-low (SL) and long-low (LL) spectrograph pointings, respectively. The regions with first and second order coverage are shown by the red and blue boxes, respectively. These regions are used for background subtraction. The orange regions have both 1st and 2nd order coverage, and the 2D spectrum of the source is extracted from these regions.

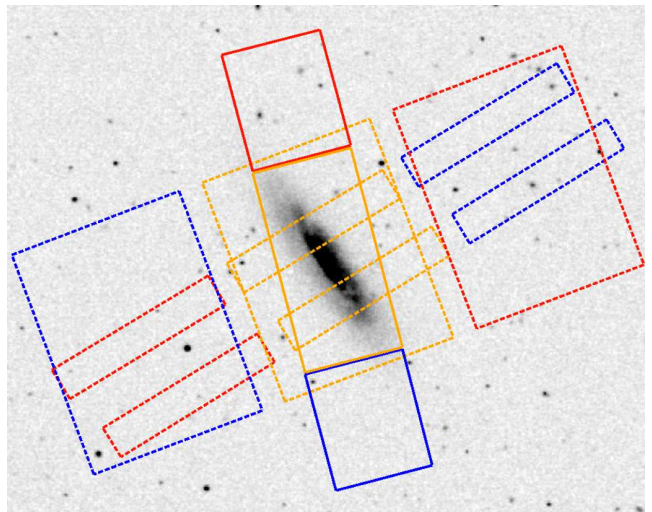


FIG. 2.— $8' \times 10'$ DSS image of NGC 4522. The solid and dashed boxes represent the short-low (SL) and long-low (LL) spectrograph pointings, respectively. The regions with first and second order coverage are shown by the red and blue boxes, respectively. These regions are used for background subtraction. The orange regions have both 1st and 2nd order coverage, and the 2D spectrum of the source is extracted from these regions. There are three sets of LL pointings shown in the image. The larger map provides a complete coverage of the galaxy and is constructed from our own observations. The two smaller maps, which are centered on regions with known signatures of ram-pressure stripping, are derived from archival data.

erage map for ESO 137-001 has already been presented in Paper 1.

The spectra presented in this paper are first extracted using a custom program that sums the spectra and root-sum-squares the errors within a specified region for each order from the SL and LL spectrographs. The code then stitches the spectra from all orders together without rescaling. The flux values within overlapping wavelength regions are interleaved. The stitched spectrum is then shifted to rest wavelengths using the optical redshift for the galaxy found in the NASA Extragalactic Database (NED). The line fluxes are derived by fitting the extracted spectrum using *PAHFIT* (Smith et al. 2007). This routine fits for all H₂ and fine structure

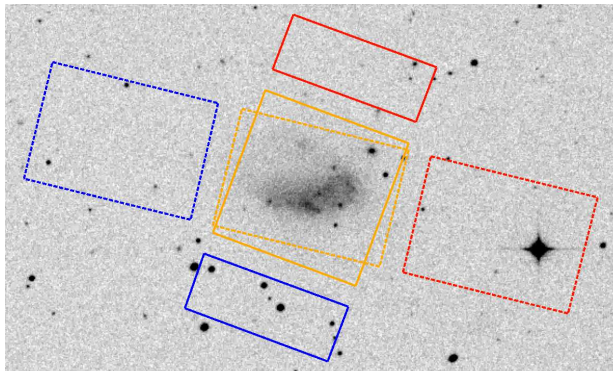


FIG. 3.— $6' \times 10'$ map digitized sky survey (DSS) image of NGC 1427A with *Spitzer* IRS pointings overlaid. The solid and dashed boxes represent the short-low (SL) and long-low (LL) spectrograph pointings, respectively. The regions with first and second order coverage are shown by the red and blue boxes, respectively. These regions are used for background subtraction. The first order LL background is partially dominated by a bright star. The slit pointings that overlap the star position are removed from the final background stack. The orange regions have both 1st and 2nd order coverage, and the 2D spectrum of the source is extracted from these regions.

lines, aromatic features, and dust continuum within the wavelengths probed by IRS. We typically do not include fitting for extinction except for the case of NGC 4522 where there is a significant amount of dust, as evidenced by the $10\mu\text{m}$ silicate absorption feature in the spectra. Strong extinction can significantly change the fluxes of S(1) thru S(7) lines. The dust extinction fitting is discussed in further detail below. The H_2 line fluxes and 1σ errors used in our analyses of the H_2 population are the values reported by the *PAHFIT* routine. To determine the contribution of PAH complexes to the spectrum, we used *PAHFIT*'s *pahfit_main_feature_power* routine to accurately determine the errors of correlated features. The H_2 , PAH feature, and fine structure line fluxes are presented in Tables 1, 2, and 3, respectively.

Two different types of H_2 images are generated for our analyses. The first does not employ any continuum subtraction. It is generated by summing the rest wavelength spectra within three wavelength bins centered on the $17.035\mu\text{m}$ H_2 ($0-0 J=3-1$ S(1)) transition. The second type of H_2 image is a continuum-subtracted version of the first. The continuum is estimated by generating two adjacent wavelength bins of the same size to the one already generated for the H_2 image and then averaging the flux between the two background bins. This method works well for fairly strong H_2 features without significant $17\mu\text{m}$ aromatic features, but it is more difficult to detect faint H_2 emission in the continuum-subtracted images due to the additional noise introduced by the subtraction.

We carry out an additional analysis step for NGC 4522 to combine our LL and archival datasets. For generating the $17\mu\text{m}$ images, we coadded the two images generated for each set of observations using the following method: First, we registered and interpolated the image generated from the deeper observations to match the pixel grid of the shallower observations. Second, in regions of coverage overlap, we calculated a weighted average of the two different datasets using the inverse variance of each dataset as weights. Third, in areas without any overlap, we kept the original value associated with the dataset

that covered the area. For the generation of spectra, if the chosen extraction region fell entirely within the region where the deeper observations were carried out, we extracted the spectra from just the deeper observations. Otherwise, we use the data from our shallower map.

We also construct $24\mu\text{m}$ images that mimic what would be observed by the *Spitzer* MIPS imager. We compute a $24\mu\text{m}$ flux with the IRS data for each sky pixel by using the MIPS $24\mu\text{m}$ transmission curve as weights.

3. RESULTS

We present our results for the four galaxies below. In the case of ESO 137-001, we only present new results that were not discussed in Paper 1. This section is organized into two parts: First, we characterize the warm H_2 emission in our galaxies. We detect significant warm H_2 emission in 97073, NGC1427A, and NGC 4522; however in the case of NGC 1427A, we have only sufficient information to place a lower limit on the warm H_2 mass. For the other two galaxies, we present the thermodynamic properties of the observed H_2 and quantify the amount of emitting gas by fitting one or two-temperature models to the excitation diagrams for H_2 within each galaxy and nearby regions of interest. Second, we present the star forming properties of these galaxies. We examine the spatial distribution of warm dust both at $8\mu\text{m}$ and $24\mu\text{m}$ for signs of ram-pressure induced star formation and determine its correspondence with $\text{H}\alpha$ emission. We measure properties such as star formation rates within the galaxies and compare them to a typical galaxy of the same stellar mass in the field. The four galaxies as an ensemble have star forming properties consistent with their being drawn from the field population. At most, only one of them shows any hint of quenching. It appears that ram-pressure stripping has not significantly impacted star formation in these galaxies.

3.1. Characterization of Warm H_2

3.1.1. CGCG 97-073

97073 is a galaxy within Abell 1367 that has a measured optical redshift of 0.024267 as reported by the NASA Extragalactic Database (NED). Abell 1367, itself, has a redshift of 0.022, also obtained from NED, which we use to calculate the approximate luminosity distance to the galaxy of 96 Mpc. The galaxy is located at a projected distance of 640 kpc from the cluster center and has a 50 kpc long collimated $\text{H}\alpha$ tail that stretches directly north of the galaxy (Gavazzi et al. 2001). In Figure 4, we show images at IRAC 3.6 and $8\mu\text{m}$, $\text{H}\alpha$ (obtained from the GOLDMine database), and rest $17.035\mu\text{m}$ (H_2 0-0 S(1) transition) wavelengths. Moreover, we show the approximate location and orientation of the faint $\text{H}\alpha$ tail, seen by Gavazzi et al. (2001) in their deep $\text{H}\alpha$ images of this galaxy, with an arrow. The IRS slit positioning captures only a small portion of the $\text{H}\alpha$ tail. The side of the galaxy thought to be interacting with the ram-pressure wind is the southernmost edge. From a comparison of the $\text{H}\alpha$, $8\mu\text{m}$, and $17\mu\text{m}$ images, it is clear that the $17\mu\text{m}$ emission does not fully match the observed $\text{H}\alpha$ and $8\mu\text{m}$ emission even after considering the effects of spatial resolution. The overabundance of $17\mu\text{m}$ emission at the tail end of the galaxy suggests the presence of warm H_2 .

TABLE 1
MEASURED H₂ ROTATIONAL LINE FLUXES

Galaxy	Region	S(0)	S(1)	S(2)	H ₂ 0-0 S(3) (10 ⁻¹⁷ W m ⁻²)	S(4)	S(5)	S(6)	S(7)
ESO 137-001 ^a	Nuclear	0.259 ± 0.087	1.47 ± 0.02	1.02 ± 0.16	2.99 ± 0.33	< 1.68	< 2.24	< 1.72	2.00 ± 0.62
	Tail (SL/LL) ^b	0.23 ± 0.01	0.92 ± 0.01	0.42 ± 0.08	1.20 ± 0.11	< 0.59	< 1.04	< 0.74	1.03 ± 0.26
	Far Tail (LL-only) ^b	0.21 ± 0.02	0.80 ± 0.09
CGCG 97-073	Full	1.62 ± 0.03	5.16 ± 0.07	1.79 ± 0.56	7.15 ± 0.89	< 6.36	< 1.23 × 10 ³	< 3.96	< 9.30
	Tail	0.50 ± 0.01	1.43 ± 0.03	0.68 ± 0.22	2.03 ± 0.28	< 1.91	< 1.69 × 10 ²	< 0.65	< 4.92
NGC 4522	Central	2.92 ± 0.09	8.82 ± 0.30	3.50 ± 1.02	8.23 ± 1.86	< 8.28	< 15.5	< 13.1	< 12.3
	NE	0.64 ± 0.07	2.00 ± 0.14	< 2.40	< 4.47	< 6.39	< 10.1	< 8.58	13.0 ± 3.8
	SW	0.87 ± 0.04	1.83 ± 0.07	< 2.24	3.68 ± 1.12	< 5.76	< 11.4	< 9.69	< 10.5
NGC 1427A	Galactic	1.16 ± 0.08	< 0.50	< 4.41	< 4.89	< 16.4	< 16.8	< 14.5	15.0 ± 4.3
	High Flux	0.81 ± 0.05	< 0.34	< 2.24	< 3.09	< 8.52	< 10.3	< 10.1	< 7.95

NOTE. — All upper limits are 3 σ .

^a See Sivanandam et al. (2010) for a description of regions.

^b The H₂ fluxes were obtained from Sivanandam et al. (2010).

TABLE 2
PAH FEATURE FLUXES

Galaxy	Region	PAH 6.2 μ m	PAH 7.7 μ m (10 ⁻¹⁷ W m ⁻²)	PAH 11.3 μ m
ESO 137-001 ^a	Nuclear	65.9 ± 1.8	215 ± 7	58.1 ± 0.9
	Tail (SL/LL)	2.22 ± 0.73	21.1 ± 2.1	3.43 ± 0.29
CGCG 97-073	Full	37.4 ± 4.5	80.2 ± 14.1	27.6 ± 1.6
	Tail	< 4.48	< 6.91	1.86 ± 0.35
NGC 4522	Central	368 ± 12	1230 ± 40	369 ± 7
	NE	< 13.5	22.6 ± 7.2	41.1 ± 3.2
	SW	< 15.5	< 34.0	45.7 ± 3.3
NGC 1427A	Galactic	39.1 ± 11.1	< 48.9	40.3 ± 4.1
	High Flux	20.6 ± 8.0	< 23.8	23.6 ± 2.2

NOTE. — All upper limits are 2 σ .

^a Refer to Sivanandam et al. (2010) for descriptions of regions.

TABLE 3
FINE STRUCTURE LINE FLUXES

Galaxy	Region	[Ne II] 12.8 μ m	[Ne III] 15.6 μ m	[S III] 18.7 μ m (10 ⁻¹⁷ W m ⁻²)	[OIV],[FeII] ^a 25.9, 26.0 μ m	[S III] 33.5 μ m	[Si II] 34.8 μ m
ESO 137-001	Nuclear	9.80 ± 0.24	1.47 ± 0.02	4.32 ± 0.04	0.45 ± 0.01	5.70 ± 0.02	8.70 ± 0.03
	Tail (SL/LL) ^b	1.17 ± 0.11	0.25 ± 0.01	0.30 ± 0.01	0.14 ± 0.01	0.87 ± 0.02	1.16 ± 0.02
	Far Tail (LL-only) ^b	...	< 0.21	0.17 ± 0.04	...	0.18 ± 0.06	0.57 ± 0.08
CGCG 97-073	Full	4.05 ± 0.77	2.76 ± 0.06	3.31 ± 0.10	0.32 ± 0.03	4.90 ± 0.04	5.46 ± 0.05
	Tail	< 0.56	< 0.09	< 0.06	0.08 ± 0.01	0.45 ± 0.02	0.60 ± 0.02
NGC 4522	Central	30.3 ± 1.46	5.56 ± 0.19	12.7 ± 0.2	4.50 ± 0.21	15.0 ± 0.2	26.4 ± 0.2
	NE	< 3.12	0.66 ± 0.17	0.58 ± 0.12	0.62 ± 0.15	1.80 ± 0.13	2.80 ± 0.16
	SW	< 2.26	0.91 ± 0.06	0.56 ± 0.08	0.14 ± 0.04	1.66 ± 0.06	2.25 ± 0.08
NGC 1427A	Galactic	< 3.63	2.01 ± 0.21	2.30 ± 0.16	< 8.36	0.99 ± 0.19	4.77 ± 0.26
	High Flux	< 2.42	0.78 ± 0.10	1.68 ± 0.11	< 18.9	< 0.38	1.88 ± 0.14

NOTE. — All upper limits are 3 σ .

^a Blended feature.

^b Flux values obtained from Sivanandam et al. (2010).

Upon closer inspection, we detect significant emission of warm H₂ within the galaxy and in a portion of its tail in the extracted spectra. We show the extracted spectra within the full galaxy extraction region and tail extraction region in Figure 5. Within the full galaxy extraction region, H₂ lines in addition to a few fine structure lines dominate the spectrum. There are significant detections of the ground state rotational H₂ S(0) to S(3) lines. In the tail extraction region, the strongest lines are H₂ lines

with the S(1) line being the strongest. What is particularly striking within this region is the large ratio of the H₂ line relative to continuum emission. It is clear that a significant fraction of the flux in the spectrum arises from H₂ line emission from the tail region. The H₂ emission of this galaxy is as dramatic as was observed in ESO 137-001, which is discussed at length in Paper 1. Bright fine structure lines, such as [NeII], [NeIII], [SIII], and [SiII],

TABLE 4
MEASURED H₂ PROPERTIES AND GAS MASSES FOR GALAXIES

Galaxy	Region	Component	T _{ex} (K)	N _{tot} (cm ⁻²)	Σ (M _⊙ pc ⁻²)	H ₂ Mass (M _⊙)
CGCG 97073	Full	Warm	130 ⁺⁶ ₋₁₂	6.6 ^{+2.0} _{-0.8} × 10 ¹⁹	1.1 ^{+0.3} _{-0.1}	4.7 ^{+1.4} _{-0.5} × 10 ⁸
		Hot	593 ⁺²³³ ₋₁₁₅	2.6 ^{+3.1} _{-1.5} × 10 ¹⁷	4.2 ^{+4.9} _{-2.4} × 10 ⁻³	1.8 ^{+2.2} _{-1.0} × 10 ⁶
	Tail	Warm	114 ⁺¹⁷ ₋₁₃	1.2 ^{+0.6} _{-0.4} × 10 ²⁰	1.9 ^{+0.9} _{-0.6}	2.1 ^{+1.0} _{-0.7} × 10 ⁸
		Hot	480 ⁺³¹⁴ ₋₄₄	6.5 ^{+3.4} _{-5.0} × 10 ¹⁷	1.0 ^{+0.5} _{-0.8} × 10 ⁻²	1.2 ^{+0.6} _{-0.9} × 10 ⁶
NGC 4522	Central	Warm	116 ⁺¹³ ₋₁₄	1.9 ^{+1.0} _{-0.5} × 10 ²⁰	3.0 ^{+1.6} _{-0.8}	3.7 ^{+2.1} _{-1.0} × 10 ⁷
		Hot	423 ⁺¹²³ ₋₄₂	1.3 ^{+0.8} _{-0.9} × 10 ¹⁸	2.1 ^{+1.3} _{-1.4} × 10 ⁻²	2.7 ^{+1.6} _{-1.7} × 10 ⁵
	NE	Warm	141 ± 2	4.0 ± 0.3 × 10 ¹⁹	0.64 ± 0.04	4.8 ± 0.3 × 10 ⁶
	SW	Warm	127 ± 2	6.4 ^{+0.6} _{-0.5} × 10 ¹⁹	1.0 ± 0.1	8.7 ^{+0.8} _{-0.7} × 10 ⁶
NGC 1427A	Galactic	Warm	< 91	> 1.2 × 10 ²⁰	> 1.8	> 5.9 × 10 ⁷
		Warm ^a	< 104	> 6.6 × 10 ¹⁹	> 1.1	> 3.4 × 10 ⁷
	High IR Flux	Warm	< 91	> 1.7 × 10 ²⁰	> 2.8	> 4.1 × 10 ⁷
		Warm ^a	< 103	> 1.0 × 10 ²⁰	> 1.6	> 2.4 × 10 ⁷

^a This assumes an OPR of 1.5.

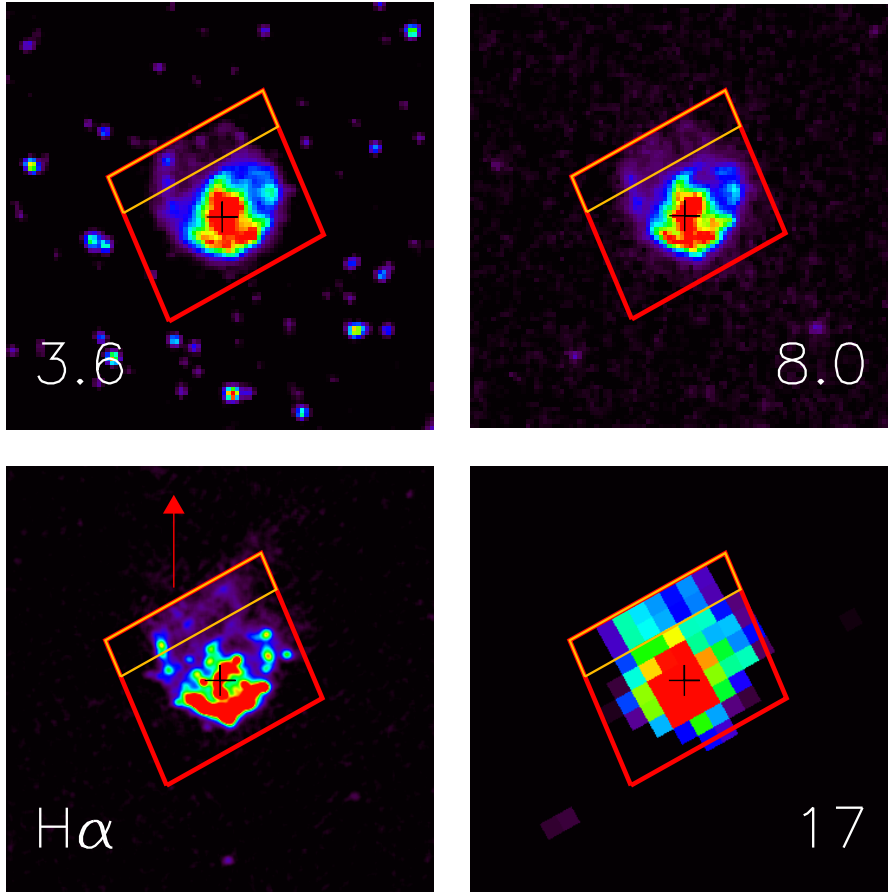


FIG. 4.— 2' × 2' images of CGCG 97-073 at 3.6 μm, 8 μm, H α (GOLDMine), and rest 17.035 μm (H₂ 0-0 S(1) transition) wavelengths. North is up and East is left. The H α image is smoothed to 1.2'' resolution. The colors follow the visible spectrum where blue represents the faintest emission and red the brightest. The center of the galaxy is shown by the black cross. The red and orange boxes represent spectral extraction regions. The red box represents the full galaxy extraction region while the orange one represents the tail extraction region. The red arrow represents the approximate location of the H α tail and its orientation with respect to the galaxy (Gavazzi et al. 2001). As noted by Gavazzi et al. (2001), there is an arc-like feature present in the H α image that is on the side of the galaxy that is directly opposite to the tail. This feature is also observed at 8 μm, which means it is star formation associated with the ISM/ICM interaction. There is possibly significant H₂ emission throughout the galaxy as indicated by the 17 μm image, including the northern edge of the galaxy, which we consider as the tail, where there is very little stellar emission as shown by the 3.6 μm image.

are also observed in both extraction regions.

We calculate the column density, temperature, and total mass of the H₂ gas in the two regions using the methods outlined in Paper 1. To calculate the column density associated with each line transition, we use solid angles, Ω , of 5.16×10^{-8} and 1.30×10^{-8} sr for the galaxy and tail extraction regions, respectively. The excitation diagrams of the H₂ ground-state rotational transitions for the two regions are shown in Figure 6. The column densities for both regions cannot be fit with a single temperature model as there appear to be multiple temperature components. This was also the case for ESO 137-001. We adopted the same two-temperature-component model discussed in Paper 1. The model (a hot and a warm component; Equation 4 in Paper 1) fits adequately for both extraction regions. The fit results are tabulated in Table 4. For the whole galaxy, we determine the warm component to have a temperature of 130^{+6}_{-12} K and a column density of $6.6^{+2.0}_{-0.8} \times 10^{19}$ cm⁻². For the hot component, we find a temperature of 593^{+233}_{-115} K and a column density of $2.6^{+3.1}_{-1.5} \times 10^{17}$ cm⁻².

The errors were estimated using Monte Carlo simulations. Because there were no additional degrees of freedom in the fit given that there are an equal number of data points as there are fit parameters, a new set of best fit model parameters was derived from each trial run. This assumed that each flux data point was Gaussian distributed with a standard deviation that was equal to its 1σ error and that the data can only be fit by a two temperature model. On the occasion where the fit failed to converge for a given trial, i.e. the two temperature model was not a good fit, that trial run was discarded. This occurs when the $\ln(N/g)$ data points are not monotonically decreasing as a function of transition temperature, which is most likely unphysical. We carried out 10,000 successful trials to determine the distribution of 1σ errors in the model parameters. The number of trials was sufficiently large to ensure the convergence of the error estimates. For all error estimations in this paper, we follow the same method.

For the tail region, we derived temperatures for the warm and hot component of 114^{+17}_{-13} K and 480^{+314}_{-44} K, respectively. These components had corresponding column densities of $1.2^{+0.6}_{-0.4} \times 10^{20}$ cm⁻² and $6.5^{+3.4}_{-5.0} \times 10^{17}$ cm⁻². The values of these fits are consistent with those derived for the full galaxy. In both cases, the warm component mass dominates over that of the hot component by a significant margin. The column densities and temperatures for H₂ in these two regions are also similar to the values obtained for the tail in ESO 137-001, suggesting that there is similar physics exciting the H₂ gas in both galaxies.

We measure a total warm H₂ mass of $4.7^{+1.4}_{-0.5} \times 10^8$ M_⊙ and $2.1^{+1.0}_{-0.7} \times 10^8$ M_⊙ within the full galaxy and tail regions, respectively. This indicates that a significant fraction of the total galaxy warm H₂ is found within the tail region. We compare the warm H₂ mass measurement with other estimates of gas masses measured for this galaxy such as cold H₂ and HI masses. In particular, we compare the warm-to-cold H₂ to look for any peculiarities. We determine the cold H₂ mass of this galaxy by using the H₂ measurement obtained

from Boselli et al. (1994) who carried out CO observations of the galaxy; we applied the appropriate distance and X_{CO} corrections to account for changes in their assumed values. Boselli et al. (1994) assumed a distance of 65 Mpc to this galaxy and used an X_{CO} value of 2.3×10^{20} cm⁻²/K-km s⁻¹. For our work, we adopt an X_{CO} of 2.8×10^{20} cm⁻²/K-km s⁻¹ from Bloemen et al. (1986), giving an H₂ mass of 1.7×10^9 M_⊙. This yields a warm-to-total H₂ mass fraction of 0.21. We assume that the aperture correction effects between the CO measurements and our H₂ measurements are not significant. This fraction is higher than the highest mass fraction value reported by Roussel et al. (2007) in their warm H₂ survey of *Spitzer* SINGS galaxies with published CO measurements. This is also a factor of two higher than the fraction of 0.1 reported by Rigopoulou et al. (2002) for starburst galaxies in their warm H₂ survey. There has been some suggestion in Stephan's Quintet that shock-heated H₂ may have an anomalously high fraction of warm-to-cold H₂ gas (Guillard et al. 2012a), which also may be the case here. We also compare the warm H₂ -to-total gas fraction of the galaxy. We adopt the HI gas mass of this galaxy of 2.0×10^9 M_⊙ measured by Scott et al. (2010). We obtain a fraction of 0.11, which is a significant fraction of the total gas within the galaxy.

We test to see if star-formation is the source of the H₂ excitation by comparing the 24 μ m image with the continuum-subtracted H₂ image. Figure 7 presents our results. The 24 μ m emission (red) is mainly confined to the part of the galaxy directly opposing the tail, presumably the location where the ICM wind hits the galaxy. The emission appears to be mainly confined to the location where most of the star formation is occurring. The blue image is the 8 μ m aromatic emission; the green image represents the continuum-subtracted H₂ S(1) transition image. The H₂ emission is clearly offset from the 24 μ m emission toward the direction of the tail.

3.1.2. NGC 4522

NGC 4522 is an infalling spiral located within the Virgo cluster and is at a projected separation of 1.1 Mpc from the cluster center. This galaxy has a large radial velocity of 1250 km s⁻¹ with respect to the cluster (obtained from NED), which suggests that a large portion of its motion is along our line-of-sight. We adopt a distance to Virgo of 16.5 Mpc (Mei et al. 2007). We present the *Spitzer* IRAC, IRS, and GOLDMine H α images of NGC 4522 in Figure 8. The 3.6 μ m image of the galaxy shows a typical unperturbed spiral. However, the H α , 8, and rest 17 μ m images reveal something completely different. Their emission is truncated compared to the radial extent of the stellar disk of the galaxy. We also see extraplanar tail-like features in the southwest quadrant of the galaxy at 8 μ m and 17 μ m, which is a clear signature of dust and possibly gas stripping. The undisturbed nature of the stellar disk indicates that ram-pressure and not tidal forces must be at play. However, this explanation is somewhat complicated by the fact that the galaxy is approximately 1 Mpc away from the Virgo cluster center and the traditional view is that the galaxy velocity and the density of the ICM at that distance cannot be sufficient to produce significant ram-pressure. However, it is likely that the relative velocity of NGC 4522 within the

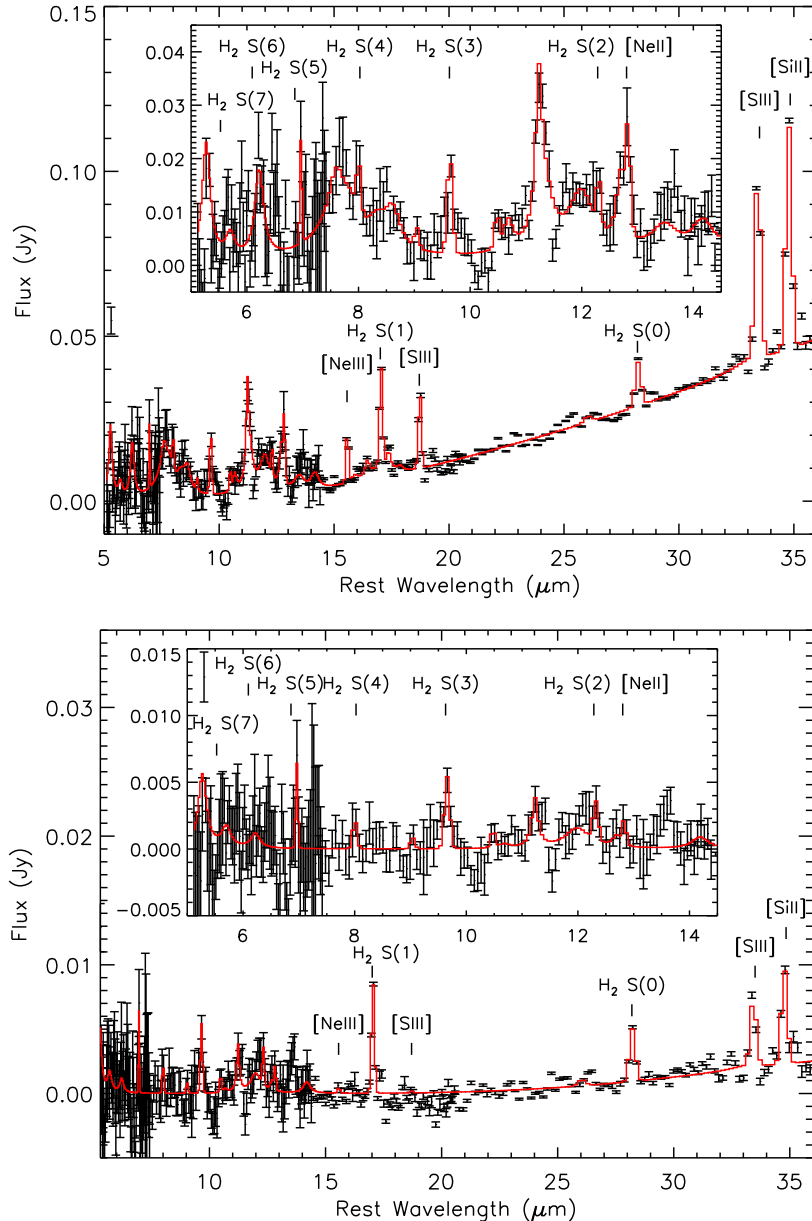


FIG. 5.— Infrared spectra of 97073 extracted from the full galaxy extraction region (top) and tail extraction region (bottom). Both spectra show significant detections of ground-state rotational H_2 lines. In both regions, the S(0) thru S(3) lines are detected. In the tail extraction region, there is significant line emission but very little continuum emission, which suggests that star formation is not the primary excitation source for H_2 in this region.

ICM is much higher than expected either because the ICM is dynamic, i.e. it is moving relative to the cluster mean velocity, and/or the galaxy is traveling at high speeds and is unbound from the cluster (Vollmer et al. 2006).

We carry out a more careful analysis by extracting spectra from key regions within the galaxy, as shown in Figure 8. In Figure 9, we present the spectra extracted from the central extraction region shown in Figure 8. We detect warm H_2 in a tail-like feature that extends approximately 4 kpc in length from the midplane of the disk along the SW extraction region. The central extraction region was defined to obtain most of the infrared emission originating from the galaxy. In it, we have significant detections of the ground-rotational level H_2 S(0)

thru S(3) lines. We also observe multiple fine structure lines and significant emission by dust, likely associated with star formation. We will explore the meaning of this observation in greater detail in Section 3.2. We also extract spectra from the northeast (NE) and southwest (SW) regions of the 17 μm emission (see Figure 8 for the exact location of the extraction regions) where the effects of ram-pressure are most obvious. The SW region spectrum was extracted from the higher signal-to-noise archival dataset. Due to the poorly constrained and unphysical value of the extinction parameter obtained by *PAHFIT*, we fixed the optical depth of the 9.7 μm silicate absorption feature to that measured for the central extraction region for the fits of the SW and NE regions. In both regions, we detect both the H_2 S(0) and S(1)

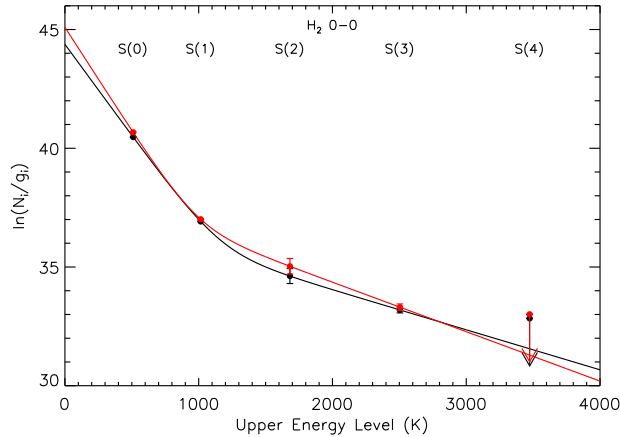


FIG. 6.— H₂ excitation diagram of 97073 for both the full galaxy extraction region (black points) and the tail extraction region (red points). The upper limits for non-detections shown are 3σ . The black and red curves are fit to the data in the full galaxy and tail regions, respectively. We fit the data with a two-temperature H₂ model and obtain a satisfactory fit for the observed line detections S(0) thru S(3) in both cases. The excitation of the gas in both regions is largely similar.

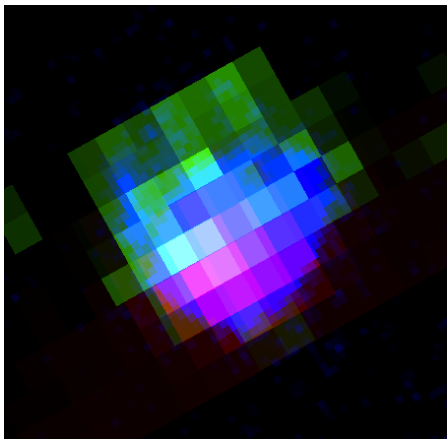


FIG. 7.— This is a color composite of 97073 seen at three difference wavelengths. The blue image is the 8 μm excess image, the green is the continuum-subtracted 17 μm H₂ image, and finally the red is the 24 μm image. There is clear offset in the H₂ emission compared to the 24 μm emission, which is associated with dust in star-forming regions.

lines. The SW region has a detection of the S(7) line while the NE region has a detection of the S(3) line. The S(7) line detection is not particularly convincing because of the increasing noise in that region. We do not include it in our model fits. It is clear that the SW region, which contains most of the observed extraplanar 17 μm emission, contains a significant amount of warm H₂. We also observe aromatic features, fine-structure lines, and dust continuum, though the relative ratio of the H₂ and dust emission appears smaller when compared to the central extraction region. We investigate the implications of this difference in further detail in Section 4.2.

To understand the physical conditions of the H₂ present in the galaxy and its tail, we fit an excitation model to the H₂ line fluxes obtained from the three different spectral extraction regions using the same methods used for 97073. The solid angles for the central, NE, and SW regions are 4.58×10^{-8} , 2.75×10^{-8} , and

3.10×10^{-8} sr, respectively. The results of these fits are also given in Table 4. For the central region, we fit a two-temperature model, which yields a warm component with a temperature of 116^{+13}_{-14} K and column density of $1.9^{+1.0}_{-0.5} \times 10^{20}$ cm⁻² and a hot component with a temperature of 423^{+123}_{-42} K and a column density of $1.3^{+0.8}_{-0.9} \times 10^{18}$ cm⁻². For the NE region, we only fit a single temperature model as we only have significant detections of two lines. We obtain a temperature of 141 ± 2 K and a column density of $4.0 \pm 0.3 \times 10^{19}$ cm⁻². For the SW region, we also fit a single temperature model due to only three significant detections of H₂ lines. We fit the S(0) and S(1) lines in this case. We obtain a temperature of 127 ± 2 K and a column density of $6.4^{+0.6}_{-0.5} \times 10^{19}$ cm⁻². The warm components of all three regions have largely consistent temperatures. We calculate a total warm H₂ mass of $3.7^{+2.1}_{-1.0} \times 10^7 M_{\odot}$, $4.8 \pm 0.3 \times 10^6 M_{\odot}$, and $8.7^{+0.8}_{-0.7} \times 10^6 M_{\odot}$ for the central, NE, and SW regions, respectively. This is an order of magnitude less warm H₂ mass than was measured for 97073. We also compare the central region warm H₂ value with the measured cold gas mass values to see if the warm-to-cold gas ratio is abnormal in any way. This galaxy has a HI mass of $3.8 \times 10^8 M_{\odot}$ (Kenney et al. 2004), and a cold H₂ mass of $3.2 \times 10^8 M_{\odot}$, derived using CO measurements (Smith & Madden 1997) corrected to our adopted distance to the galaxy and X_{CO} . This corresponds to a warm-to-cold H₂ fraction of 0.15 and a warm-to-total gas fraction of 0.06. This is largely consistent with what is observed in the SINGS sample with warm and cold H₂ measurements (Roussel et al. 2007).

We looked for kinematic signatures of the warm H₂ gas being stripped permanently from the galaxy. The galaxy has a high enough recessional velocity with respect to the cluster average that, if the stripped gas were to be permanently lost to the cluster, then the velocity shift of a spectral line should be observable by the IRS low resolution spectrographs. We chose the 17.035 μm S(1) line for this measurement. We use two different extraction regions along the H₂ tail detected in the SW region: one close to the galactic disk and one farthest away along the tail where a reliable line detection can be obtained. The extraction regions are shown in the 17 μm image in Figure 8 as cyan boxes. The continuum-subtracted line profiles from each of these regions are shown in Figure 12. There is a clear blueward shift of the S(1) line as one moves from just outside of the disk of the galaxy to the farthest reaches of the detected tail.

We carry out a gaussian fit to the line profile of each extraction region to quantify the shift in velocity. The fit velocity and FWHM parameters are $v = 720 \pm 170$ and $\Delta v = 2190 \pm 280$ km s⁻¹ for the region close to the disk. For region along the tail, we obtain fit values of $v = -740 \pm 260$ and $\Delta v = 1510 \pm 490$ km s⁻¹. This gives a relative velocity difference of $\sim 1460 \pm 310$ km s⁻¹. The relative shift in velocity is in the right direction and magnitude if the gas is lost permanently from the cluster because the measured relative velocity of the galaxy with respect to the cluster mean is 1250 km s⁻¹. To further check the validity of the shift, we investigate the properties of the IRS spectrograph used for these detections. The spectral resolutions of the low resolution spectrographs are not fixed and vary with wavelength.

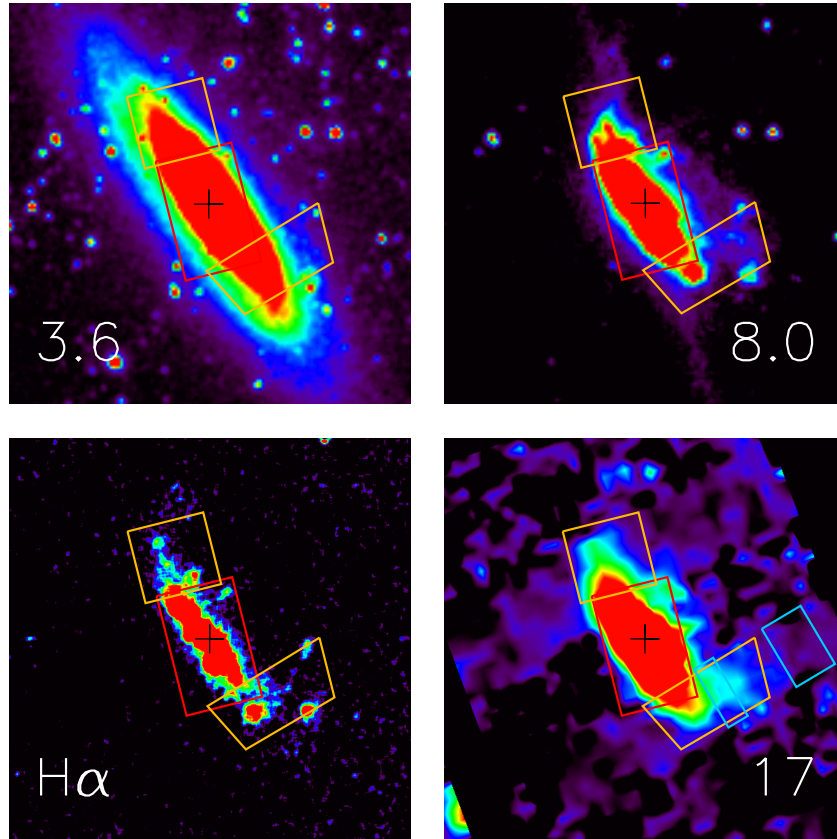


FIG. 8.— $2' \times 2'$ images of NGC 4522 at $3.6 \mu\text{m}$, $8 \mu\text{m}$, $\text{H}\alpha$ (obtained from GOLDMine), and rest $17.035 \mu\text{m}$ (H_2 0-0 S(1) transition) wavelengths. North is up and East is left. The colors follow the visible spectrum where blue represents the faintest emission and red the brightest. The center of the galaxy is shown by the black cross. The red, orange, and blue boxes represent spectral extraction regions. The red box is the central extraction region, the orange ones the NE and SW regions where ram-pressure stripping is occurring, and finally the blue extraction region is used to study the kinematics of the stripped gas. Even though at $3.6 \mu\text{m}$ this galaxy looks like a typical spiral, there are strong asymmetries observed at $\text{H}\alpha$, 8, and $17 \mu\text{m}$. Warm dust is being blown out of the galaxy as seen by the dust trails at $8 \mu\text{m}$. The $17 \mu\text{m}$ image was generated by coadding both our LL and archival LL observations. It is dominated by both the $17 \mu\text{m}$ aromatic feature and the H_2 line, so it is difficult to ascertain if there are locations with anomalously high H_2 emission. However, a tail-like feature is observed within the SW orange extraction region.

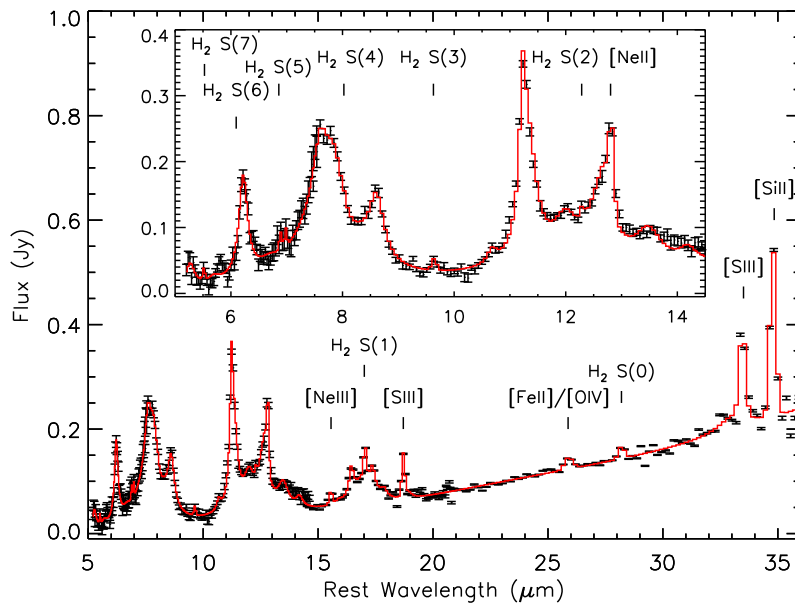


FIG. 9.— Infrared spectrum of NGC 4522 extracted from the central extraction region (shown as the red box in Figure 8). The spectrum shows significant detections of ground-state rotational H_2 lines. The S(0) thru S(3) lines are detected.

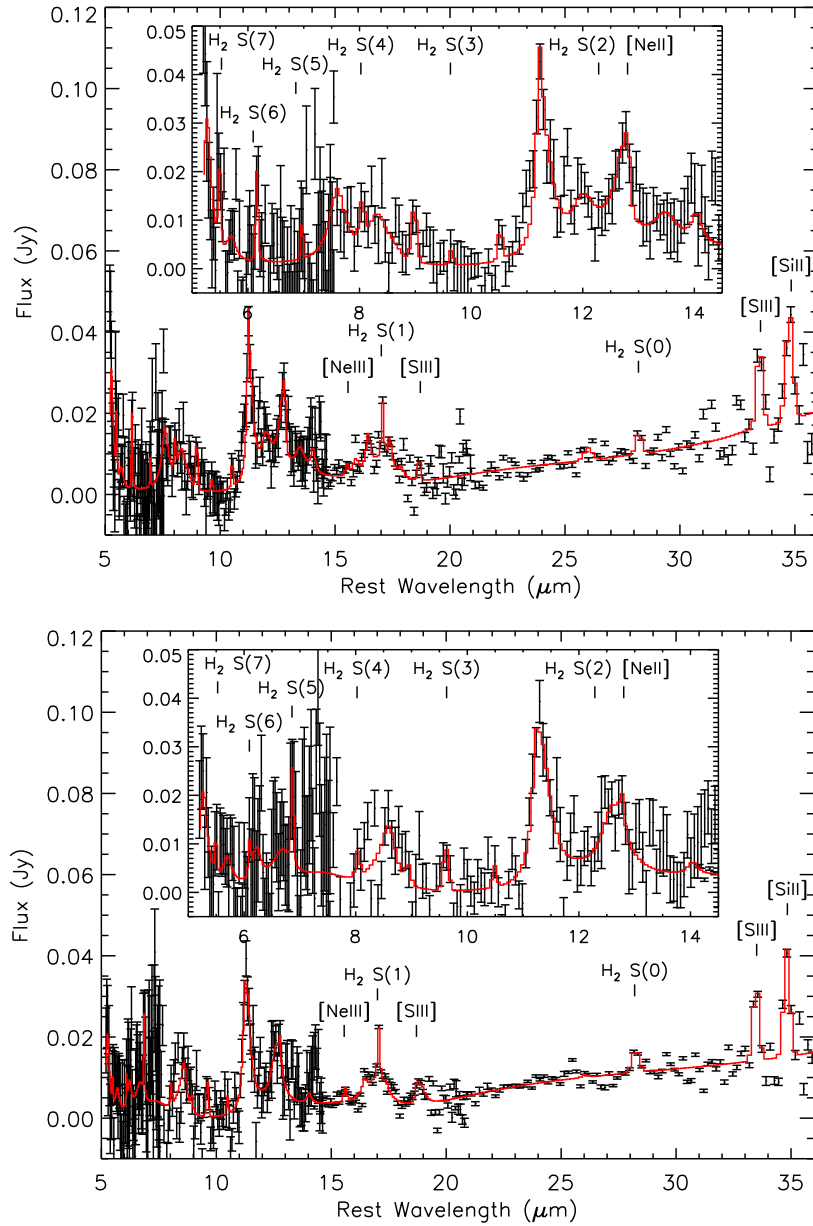


FIG. 10.— Infrared spectra of the NE and SW regions in NGC 4522 (shown as orange boxes in Figure 8) where ram-pressure is thought to be stripping gas. The top plot shows the spectrum extracted from the NE extraction region while the bottom plot shows the spectrum extracted from the SW part of the galaxy. Significant detections of the H₂ S(0) and S(1) lines are observed.

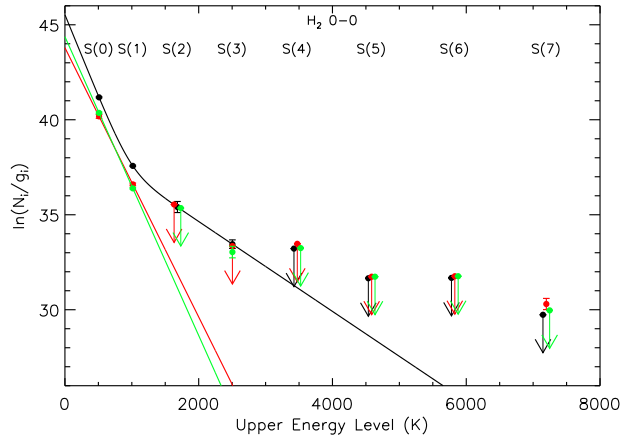


FIG. 11.— H_2 excitation diagram for NGC 4522 for three different extraction regions. The black points represent the H_2 in the central region of the galaxy. The red points are for the NE region, and the green ones are for the SW region. The upper limits for non-detections shown are 3σ limits. The limits for the three different regions are offset from each other to improve readability. We fit a two temperature component model for the data from the central region to account for the changing slope in the excitation diagram. The best fit model is shown by the black curve. For the NE and SW region, we fit a one temperature model because we only have firm detections of the S(0) and S(1) lines. The NE and SW regions do have a detection of a higher excitation line, but at least four lines are required to fit a two temperature model. The best fit models for the NE and SW regions are shown by the red and green lines, respectively.

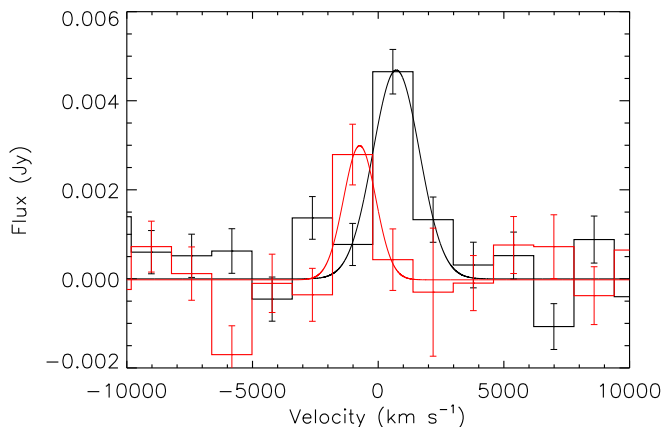


FIG. 12.— Continuum-subtracted line profiles of the H_2 S(1) line at two different locations in the stripped tail of NGC 4522. The galaxy’s line-of-sight velocity is set to be zero. An object with negative velocity means that it is moving away from the galaxy toward us. The black histogram is the line profile for a region of the tail closest to the galaxy whereas the red histogram is the line profile for a location in the tail that is further away from the galaxy. The solid curves represent the respective gaussian line profile fits. There is a clear velocity shift in the H_2 emission as one moves further away from the galaxy. The gas further away from the galaxy has a lower line-of-sight velocity. The velocity offset is consistent in direction and magnitude to the velocity difference between the galaxy and the cluster mean. This means that the gas may be being stripped permanently from the galaxy.

The spectral resolution at the $17\ \mu\text{m}$ line with the LL2 spectrograph is approximately 100. This corresponds to a velocity width of an unresolved line of $\sim 3000\ \text{km s}^{-1}$, with two pixels per resolution element. With these spectrograph characteristics and our achieved signal-to-noise one should be able to detect a shift of approximately a quarter of a line width, which corresponds to a velocity of $750\ \text{km s}^{-1}$. This value is slightly larger than the wavelength uncertainty in the calibration of $600\ \text{km s}^{-1}$. We conclude that we may have detected a velocity shift. No other mid-IR line, such as H_2 S(0) or [SiII] $34.8\ \mu\text{m}$, could be identified in the extraction region farthest from the galaxy to confirm this result. If this tentative result is correct, some of the stripped gas is being permanently lost to the ICM. Other measurements that might confirm this interesting result are inconclusive. Kenney et al. (2004) also see a blueshift in their Very Large Array (VLA) HI measurements of the stripped extraplanar gas in this galaxy. However, the blueshift is only modest, at the level of $10 - 20\ \text{km s}^{-1}$, and does not extend as far from the galactic plane as our measurement. CO observations were carried out by Vollmer et al. (2008), but they are even less extended than the HI map.

3.1.3. NGC 1427A

NGC1427A is a dwarf irregular galaxy within the Fornax cluster with arc-like stellar morphology. The galaxy has a moderate line-of-sight velocity with respect to the cluster mean of $650\ \text{km s}^{-1}$ (reported by NED). We adopt a distance of 20.0 Mpc to the cluster measured using the surface-brightness fluctuation technique (Blakeslee et al. 2009). The galaxy is at a projected separation of 130 kpc from the cluster center. We present the *HST* $\text{H}\alpha$, *Spitzer* $3.6\ \mu\text{m}$, $8\ \mu\text{m}$, and rest $28.2\ \mu\text{m}$ images in Figure 13. The $28.2\ \mu\text{m}$ image is presented instead of a $17\ \mu\text{m}$ image because no significant emission was detected at $17\ \mu\text{m}$. The $28.2\ \mu\text{m}$ image wavelength is centered on the H_2 S(0) line and also contains dust continuum emission associated with star formation. We did not subtract the dust continuum due to the low signal-to-noise detection of the S(0) line in each spaxel. The *HST* $\text{H}\alpha$ image has been smoothed to reveal the HII regions within the galaxy better. The arc-like star formation morphology seen at $8\ \mu\text{m}$ and $\text{H}\alpha$ and filamentary star forming regions seen at the western side of the galaxy at $8\ \mu\text{m}$ cannot be explained purely by a tidal mechanism and must require ram-pressure stripping. A tidal mechanism would affect the entire galaxy, but star formation is restricted to the periphery of the galaxy where the interaction between the ISM and the ICM is the greatest. The bulk of the $28.2\ \mu\text{m}$ emission is mainly centered on the part of the star-forming arc on the south side of the galaxy in an area where there is comparatively much more star formation than the rest of the galaxy. Other sources of $28.2\ \mu\text{m}$ emission within the galaxy seem to coincide with the peaks in $8\ \mu\text{m}$ emission.

We search for signatures of warm H_2 within this galaxy by extracting spectra from two different regions; the dimensions and locations of the extraction regions are shown in Figure 13. We extract spectra from a region that covers most of the galaxy and one that focuses primarily on the high IR flux region within the galaxy. The extracted spectra for each region are shown in Figure

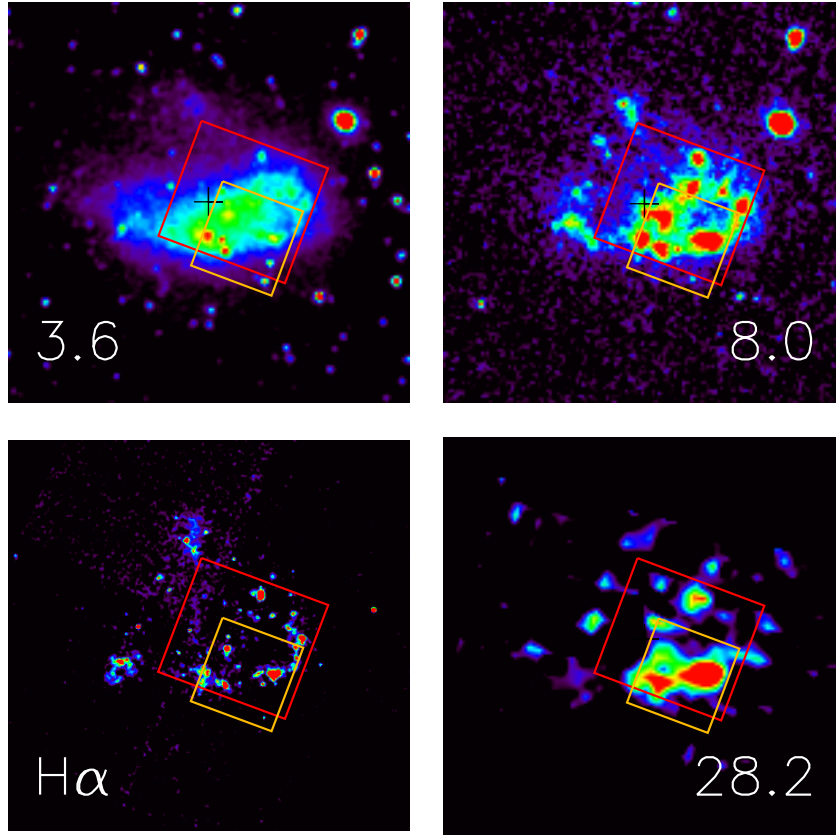


FIG. 13.— $2' \times 2'$ images of NGC 1427A at $3.6 \mu\text{m}$, $8 \mu\text{m}$, *HST* $\text{H}\alpha$, and rest $28.2 \mu\text{m}$ (H_2 0-0 S(0) transition) wavelengths. North is up and East is left. The colors follow the visible spectrum where blue represents the faintest emission and red the brightest. The center of the galaxy is shown by the black cross. The $\text{H}\alpha$ image has been smoothed to better reveal the HII regions. The red box is the spectral extraction region used to generate the spectrum for this galaxy. The $3.6 \mu\text{m}$ image shows the arc-like morphology of this galaxy. Both the $\text{H}\alpha$ and $8 \mu\text{m}$ image show star forming regions arranged along this arc. The $28.2 \mu\text{m}$ image contains both warm dust continuum and H_2 S(0) emission. The brightest regions at $28.2 \mu\text{m}$ are associated with areas of the most intense star formation in the galaxy.

14. The S(0) line is clearly detected in both regions, but there is no hint of the S(1) line; this galaxy is the only one in our sample without a firm detection of the S(1) line. In comparison, the S(1) line is the strongest H_2 line in units of flux density observed in the other three galaxies. Because the signal-to-noise ratios of the spectra for this galaxy are low, it is worth putting this result in context. The $3\text{-}\sigma$ upper limit to the S(1) to S(0) line ratio is unusually low with a value ≤ 0.4 . The typical values of the line flux ratio measured in other galaxies in our sample fall in the 2 – 6 range, so this upper limit is a factor of 5 less than the lowest ratio we measure in our sample.

Given that our sample is relatively limited, it may not be unusual to find systems with such a low line ratio in a larger sample with measured H_2 rotational line fluxes, such as the SINGS galaxies (Roussel et al. 2007). The SINGS sample has a median line flux ratio of 3.1, which falls well within the range of values observed in the remaining three galaxies in our sample. However, there are three SINGS systems with unusually low S(1)/S(0) ratios (i.e. < 1.0): NGC 24, NGC 1705, and NGC 4552. All three of these systems have low ortho-to-para ratios ($0.5 < \text{OPR} < 1.5$) with warm gas component temperatures ($78\text{K} < T < 127\text{K}$) on the low end of the observed distribution in all sample galaxies. Two of these galaxies, NGC 24 and NGC 1705, are dwarfs and also have com-

parably low S(1)/S(0) ratios of 0.3 – 0.4. The fact that we do not see the S(1) line in NGC 1427A can mean two things: (1) The warm H_2 within NGC 1427A is cooler than the gas found in the other three galaxies in our sample; and/or (2) The ortho-to-para ratio (OPR) for the H_2 gas is lower than our assumed value of 3. Typically, the critical densities of the S(1) and S(0) transitions are low enough that they are thermalized in most galaxies. However, if the gas density is sufficiently low, the even and odd states of H_2 remain decoupled and the ortho-to-para ratio of the H_2 gas is essentially set to the value of the gas when it initially formed. Roussel et al. (2007) suggest in their work that this may explain the low observed OPR values in the three galaxies in their sample.

We construct a H_2 excitation diagram, Figure 15, for the two regions from which the spectra have been extracted. The solid angles of the galactic and high IR flux regions are 7.96×10^{-8} and 3.71×10^{-8} sr, respectively. The column density values shown in the diagram assume a nominal OPR of 3. We can place constraints on the total warm H_2 mass detected within the two extraction regions by using the detection of the S(0) and the 3σ detection limit for the S(1) line. To explore the effects of the OPR, we compute H_2 mass estimates for corresponding values of 1.5 and 3 using a single temperature model. The results of these fits are given in Table 4. The fit within the galactic extraction region yields a temper-

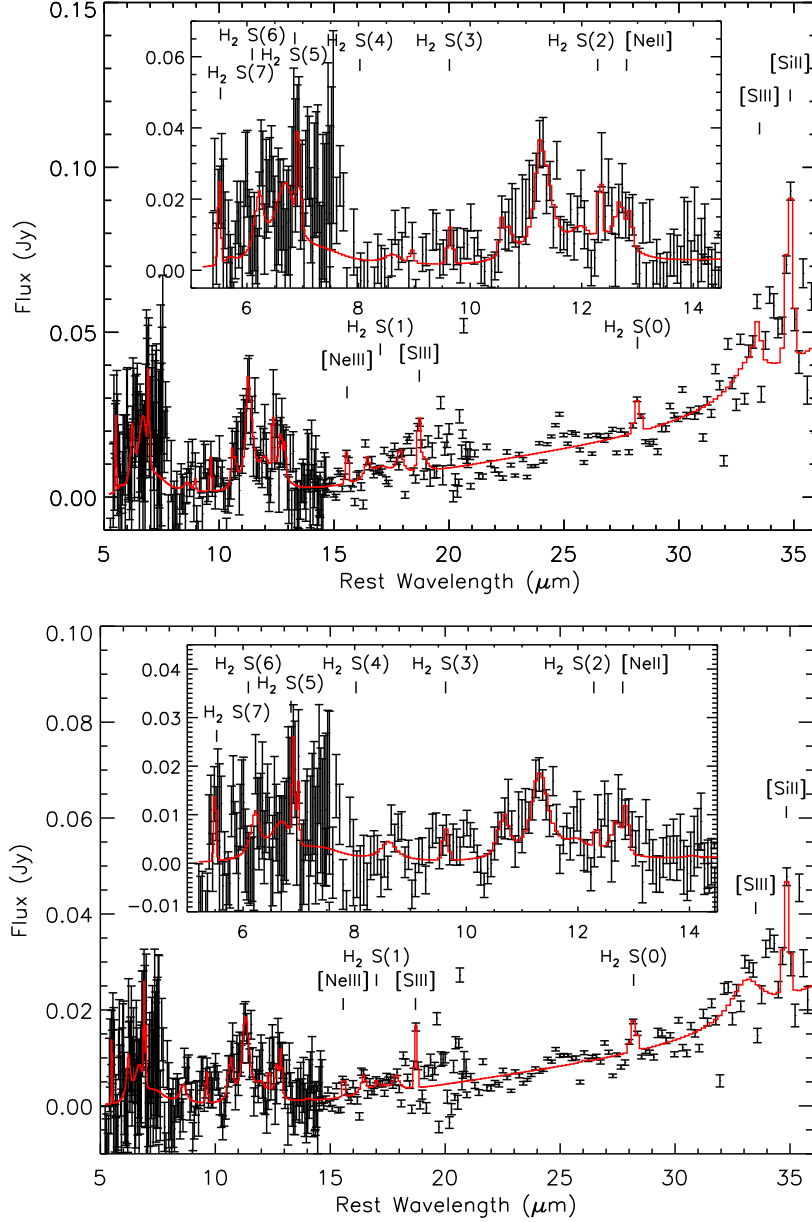


FIG. 14.— Infrared spectra of NGC 1427A extracted from the galaxy extraction region (top) and the high IR flux region (bottom). There is only a significant detection of warm H₂ is the S(0) transition in both regions. The S(1) line is noticeably absent suggesting the temperature of the warm H₂ component is lower than what is generally expected and/or the ortho-to-para ratio is lower than 3.

ature upper limit of 91K and a H₂ column density lower limit of $1.2 \times 10^{20} \text{ cm}^{-2}$. Similarly, the high IR flux region is best fit by a temperature of $< 91\text{K}$ and an H₂ column density of $> 1.7 \times 10^{20} \text{ cm}^{-2}$. The temperature is a few tens of Kelvin cooler than the warm component temperature observed in the other three galaxies in our sample, but is consistent with the values derived from galaxies exhibiting low S(1)/S(0) ratios in the SINGS sample. This yields a H₂ mass lower limit of $4.7 \times 10^7 M_{\odot}$ and $5.9 \times 10^7 M_{\odot}$ for the high IR flux and galactic regions, respectively. These results indicate that most of the H₂ mass is concentrated within the high IR flux region where there is significant star formation. For an OPR of 1.5, we obtain an upper limit to the temperature of 104K and a lower limit to the column density of $6.6 \times 10^{19} \text{ cm}^{-2}$ for the galactic region. This in turn translates into a lower limit

on the warm H₂ gas mass of $3.4 \times 10^7 M_{\odot}$, which is a 40% reduction in mass compared to the OPR=3 case. For the high IR flux region, we obtain the corresponding temperature upper limit and column density lower limit of 103K and $1.0 \times 10^{20} \text{ cm}^{-2}$. This yields a warm H₂ mass upper limit of $2.4 \times 10^7 M_{\odot}$. There is a possibility that even lower OPR values may apply to the H₂ gas within NGC 1427A. This would push the upper limit of the temperature even higher than what has been found with our analysis while reducing the lower limit on the total mass.

Without a firm detection of the S(1), S(2), and S(3) lines, it is impossible to constrain the OPR ratio. We will conservatively assume that the lower limit to the H₂ mass of NGC 1427A to be $3.4 \times 10^7 M_{\odot}$. To set a reasonable upper bound on the warm H₂ mass, we compute

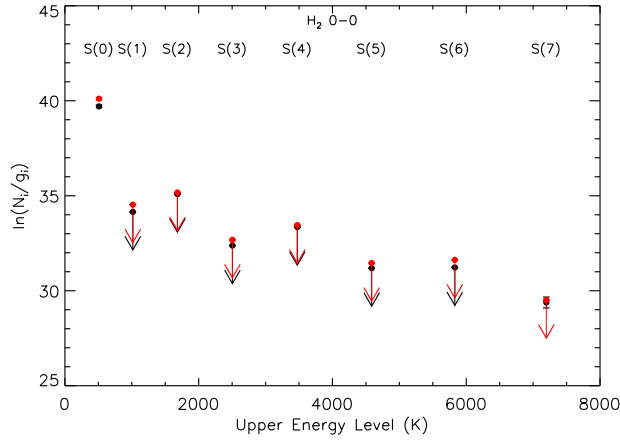


FIG. 15.— H₂ excitation diagram for NGC 1427A. The black and red points represent the values obtained from the galactic and high IR flux extraction regions, respectively. All upper limits are 3σ limits. In both the galactic and high IR flux extraction regions, we have a significant detection of the S(0) line. The S(7) line is also detected in the galactic extraction region, but no other H₂ lines are detected in the high IR flux region. There are insufficient line detections to reliably determine the temperature of the warm H₂ gas. The non detection of the S(1) may be the result of either lower than usual warm component temperature and/or a lower OPR value for the gas.

the mass using the lowest temperature of warm H₂ gas observed in the SINGS sample of 78K. It is worth noting that this temperature is observed in NGC 1705, which is one of the dwarf low OPR galaxies discussed above. This temperature choice yields a value of $1.3 \times 10^8 M_{\odot}$. We compare this with the published value of HI mass of $3.3 \times 10^9 M_{\odot}$ (Koribalski et al. 2004). The ratio of warm H₂ to HI has lies in the range ~ 0.01 to ~ 0.04 . This limit is lower than what has been observed in 97073 and NGC 4522, suggesting that there is nothing unusual about the warm H₂ emission observed in NGC 1427A and it may just be produced by star forming activities. In the discussion, additional evidence involving the H₂-PAH flux ratio further substantiates this conclusion.

3.2. Dust and Star-Forming Properties

In this section, we study the star forming properties of the galaxies within our full sample and present the results of individual galaxies in the sections below. All galaxies show significant star forming activities and marked asymmetries in their distribution of star forming regions. We will not discuss the star forming properties of ESO 137-001 as it has already been discussed in detail in Paper 1. To understand star formation better in these ram-pressure stripped galaxies, we present the $8 \mu\text{m}$ excess images in Figure 16 and IRS-derived $24 \mu\text{m}$ images in Figure 17. Even though both bands trace star formation, their utility to our analysis varies. $8 \mu\text{m}$ emission offers a high resolution view of the morphology of star forming activities, but it is a poor indicator of the star formation rate. $24 \mu\text{m}$ emission has poorer spatial resolution compared to $8 \mu\text{m}$, but it is well calibrated to provide accurate measures of star formation rates within the galaxies in question. Therefore, these bandpasses offer a complementary view of star forming activities.

Thus, we have two goals. The first is to probe any effects of the ICM on star formation by comparing the

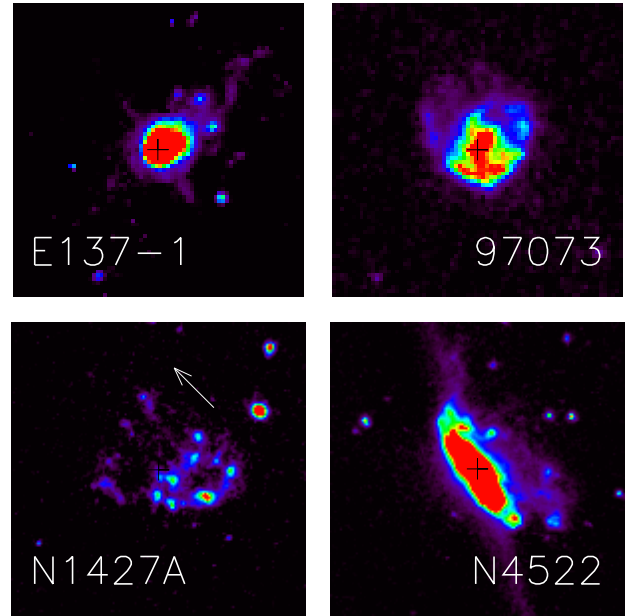


FIG. 16.— $8\mu\text{m}$ excess images of ESO 137-001, CGCG 97-073, NGC 1427A, and NGC 4522 that reveal the aromatic dust emission from these galaxies. The images of ESO 137-001 and 97073 are 30×30 kpc in size, while the images of NGC 1427A and NGC 4522 are 15×15 kpc in size. The black crosses represent the centers of the galaxies. The image of ESO 137-001, already published in Paper 1, shows asymmetric dust emission at the galactic center and extraplanar $8\mu\text{m}$ emission, which have been confirmed to be star-forming regions. In the case of NGC 1427A, the direction of the star formation trails is shown by a white arrow.

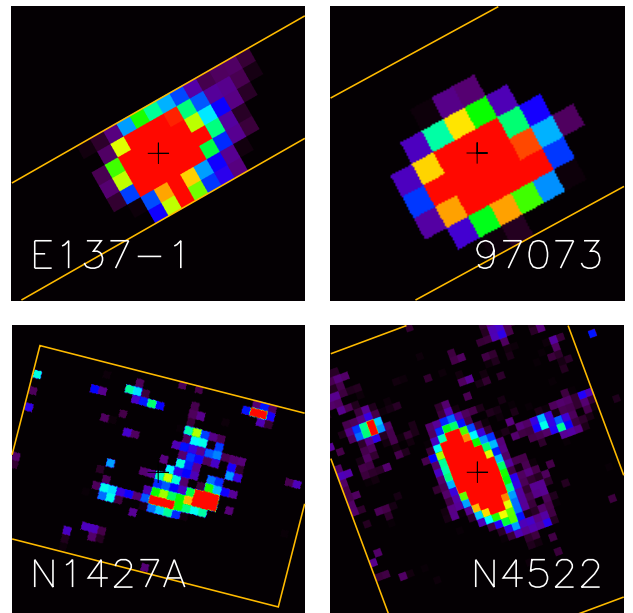


FIG. 17.— $24 \mu\text{m}$ images of ESO 137-001, CGCG 97-073, NGC 1427A, and NGC 4522 generated from IRS spectral cubes. The images of ESO 137-001 and 97073 are 30×30 kpc in size, while the images of NGC 1427A and NGC 4522 are 15×15 kpc in size. The orange lines show the IRS coverage and the corresponding extents of the $24 \mu\text{m}$ images. The $24 \mu\text{m}$ emission is produced by warm dust emission associated with star formation. The observed intensity distribution matches well with excess $8 \mu\text{m}$ emission when the lower resolution and spatial sampling of the $24 \mu\text{m}$ image are taken into account.

morphology at $8\ \mu\text{m}$ with the understanding of the stripping process from the H_2 behavior. The second is to see if the overall level of star formation in these galaxies is suppressed. This second issue has been examined for other cluster galaxies by Tyler et al. (2013). They find that the majority of star-forming galaxies in dense clusters fall close to the field galaxy SFR/mass relation. That is, if one takes the field relation and the width of the field distribution around this relation (FWHM ~ 1.2 dex, Brinchmann et al. (2004)), only a small minority of cluster galaxies fall significantly below expectations for field galaxies of similar mass.

3.2.1. CGCG 97-073

We confirm previous observations that the majority of the star formation is confined to one side of the galaxy, specifically the side opposite the $\text{H}\alpha$ tail (Gavazzi et al. 2001). The arc-shaped star forming region observed by Gavazzi et al. (2001) at $\text{H}\alpha$ (see Figure 4) is also seen in our $8\ \mu\text{m}$ excess image of the galaxy. In fact, the $\text{H}\alpha$ and $8\ \mu\text{m}$ emission are virtually identical with the exception of the 50 kpc tail and a northern spur observed at $\text{H}\alpha$. Significant $24\ \mu\text{m}$ emission is also detected from this galaxy. The $24\ \mu\text{m}$ emission is offset towards the direction with significant star formation and the emission is centered on the area where the greatest amount of emission is seen in both $\text{H}\alpha$ and $8\ \mu\text{m}$. Our observations strengthen the original hypothesis proposed by Gavazzi et al. (2001) that the galaxy is interacting with the ICM on its southern edge and that ram-pressure is compressing the molecular gas on that edge and promoting increased star formation along an arc-like star forming region. This is further supported by the lack of a similar feature at $3.6\ \mu\text{m}$. No obvious extraplanar star-forming regions or dust trails are seen at $8\ \mu\text{m}$ like those observed in ESO 137-001. However, it is important to note that the galaxy and its orbit may be highly inclined to our line-of-sight due to its asymmetric morphology and high line-of-sight velocity with respect to the cluster mean ($v_{gal} = 680\ \text{km s}^{-1}$) compared to the cluster velocity dispersion of $891\ \text{km s}^{-1}$ determined by Cortese et al. (2004).

We measure the *MIPS* $24\ \mu\text{m}$ flux for the two spectral extraction regions for the galaxy. We use the same techniques discussed in Paper 1 to calculate the equivalent *MIPS* $24\ \mu\text{m}$ signal from the extracted IRS spectra. However, we use a slightly different error estimation technique to quantify the error in the flux measurement because our previous error estimation technique was far too conservative. The random errors derived from the *CUBISM* generated spectra do not reflect the fluctuations present in the IR continuum due to systematic errors that arise from the reduction. We attempt to quantify properly the error by following these steps: (1) We focus on the $20 - 30\ \mu\text{m}$ spectral range, as that is roughly the *MIPS* $24\ \mu\text{m}$ bandpass, and we remove any spectral lines present, namely the $28.2\ \mu\text{m}$ S(0) line; (2) We carry out a polynomial fit to the spectrum and subtract the fit from the spectrum to remove the smooth component associated with the continuum; and (3) We estimate the scatter about the mean by computing the standard deviation of the subtracted spectrum. We take the error for each flux data point within the $20 - 30\ \mu\text{m}$ range to be the scatter computed in step 3. The calculation of the

MIPS $24\ \mu\text{m}$ flux involves taking the weighted average of the $20 - 30\ \mu\text{m}$ spectrum using the *MIPS* relative response curve as weights. We calculate the error in the $24\ \mu\text{m}$ flux value accordingly using the relative response curve weights as given in the following equation:

$$\sigma_{f24} = \left[\frac{1}{\sum_j c_j} \sum_i (c_i \sigma_{f,i})^2 \right]^{\frac{1}{2}} \quad (1)$$

where σ_{f24} is the error in the $24\ \mu\text{m}$ flux, c_i is the *MIPS* relative response value computed at each wavelength value in the IRS spectrum, and $\sigma_{f,i}$ is the flux error for each IRS data point, which we take to be the scatter value computed above. We apply this method to all of the galaxies in our sample.

We measure $24\ \mu\text{m}$ fluxes of $18.8 \pm 0.3\ \text{mJy}$ and $0.30 \pm 0.09\ \text{mJy}$ for the galaxy and tail extraction regions of 97073, respectively. To determine the star formation rate (SFR) of the galaxy, we use both the $\text{H}\alpha$ and $24\ \mu\text{m}$ flux measurements to account for obscured and unobscured star formation. Iglesias-Páramo et al. (2002) measure an $\text{H}\alpha$ flux of $1.55 \times 10^{13}\ \text{ergs s}^{-1}\ \text{cm}^{-2}$. It is worth noting that this measurement also includes the [NII] lines because the $\text{H}\alpha$ flux was measured through narrowband photometry. However, for irregular galaxies the [NII]/ $\text{H}\alpha$ ratio is very low (< 0.1) (Kennicutt & Kent 1983), so we do not correct for this. Using the calibration derived by Calzetti et al. (2010), we derive a SFR of $1.2\ M_{\odot}\ \text{yr}^{-1}$. Next, we determine if the galaxy's SFR is unusual in any way for its stellar mass. We estimate the stellar mass using the stellar mass-to-light ratio from the *K*-band magnitude and *B - V* colour of the galaxy along with the Bell et al. (2003) mass-to-light ratio relation. 97073 has a *K*-band apparent magnitude of 12.99 and a *B - V* colour of 0.43 (Gavazzi & Boselli 1996). This translates to a mass-to-light ratio of 0.71 and a corresponding stellar mass of $8.7 \times 10^9 M_{\odot}$. We calculate a specific star formation rate (SSFR, $\log(\text{SFR}/M_{\star} [\text{yr}^{-1}])$), of -9.9 . This falls within the normal star forming sequence for field galaxies (Tyler et al. 2013). This could mean two things: (1) The cluster environment has not yet had time to quench the star formation of this galaxy; (2) Ram-pressure has induced star formation that has increased the SSFR of the galaxy as evidenced by arc-like star forming region observed in the galaxy. For a further discussion on this topic see Section 4.1.

3.2.2. NGC 4522

Like ESO 137-001, NGC 4522 is a spectacular example of how ram-pressure can strip dust and induce extraplanar star formation. In Figure 16, the $8\ \mu\text{m}$ excess image shows evidence for significant dust stripping. The $8\ \mu\text{m}$ dust disk is much smaller than the stellar disk, hinting that dust at larger radii has already been blown off due to ram-pressure stripping. This is consistent with the outside-in picture of how ram-pressure first strips the least dense gas at larger radii as it is not as well-bound and then moves inwards as the ram-pressure strength increases. On the western side of the galaxy, there is clear evidence for dust being blown out of the disk. The most spectacular feature is the one on the southwest end of the galaxy where the largest amount of extraplanar excess $8\ \mu\text{m}$ emission is observed. The excess $8\ \mu\text{m}$ emis-



FIG. 18.— A three-color composite image of NGC 4522. North is up and East is left. Blue is *HST* F435W data, green is *HST* F814W data, and finally red is IRAC 8 μm excess emission data. This image clearly shows that there is significant amount of dust stripping occurring in this galaxy. There are a few extraplanar 8 μm excess sources that are either offset from their optical counterparts in the direction of the ICM wind or with no optical counterparts at all in the stripped dust trail immediately west of the southern end of the galaxy.

sion extends approximately 3.5 kpc from the mid-plane of the galactic disk, similar to the distribution of extraplanar warm H₂ emission. In addition to the diffuse dust emission at this location, we also see large clumps, presumably associated with star forming regions, as they are also seen at H α . The diffuse extraplanar dust emission is also visible at 24 μm , but we do not observe the clumps seen at 8 μm and H α . This may be due to a combination of reduced resolution and sensitivity at 24 μm . This observation clearly shows that dust is also significantly affected by ram-pressure and can exist some distance from the plane of the galaxy. Similar behavior was also observed in the case of ESO 137-001 where 8 μm excess sources were seen past the tidal radius of the galaxy, though the dust seen here does not extend that far. The morphology of the dust also reveals the turbulent nature of ram-pressure stripping.

We search for optical counterparts for the stellar-continuum subtracted 8 μm emission with a particular focus on the areas with extraplanar dust. We present the color composite of *HST* F435W, F814W, and *Spitzer* 8 μm excess emission in Figure 18. The large dusty clumps located immediately west of the galaxy show some blue star forming knots associated with them, but the dust emission is slightly offset to the west. There is a single 8 μm source located at the western edge of the frame that has no optical counterpart. It is unclear if the source is associated with the galaxy, though it could possibly be an extraplanar star forming region. Searches within a number of catalogues (NED, SIMBAD, and VIZIER) yielded no matches to this source.

We measure the 24 μm flux within the central, NE, and SW regions and obtain 102.8 ± 1 , 6.6 ± 0.6 , and

8.0 ± 0.3 mJy, respectively. Using the measured H α flux of 4.2×10^{-13} erg cm⁻² s⁻¹ (Gavazzi et al. 2006) and the 24 μm flux within the central extraction region, we obtain a star formation rate for the galaxy of $0.12 M_{\odot} \text{ yr}^{-1}$. The extraction apertures for the H α and 24 μm measurements do not match exactly, but they should contain most of the flux observed at these two wavelengths. We crosscheck the measured star formation rate using 100 μm *Herschel Space Telescope* photometry of this galaxy (Davies et al. 2012). Using the 100 μm flux-SFR relation from Rieke et al. (2009), we convert a 100 μm flux density of 5.12 Jy to a SFR of $0.16 M_{\odot} \text{ yr}^{-1}$, which is consistent with our original measurement. The 100 μm -derived SFR is slightly larger because the *Herschel* measurement covers the entire galaxy while we only consider the central extraction region. To be consistent with other galaxies in our sample, we only use the H α /24 μm -derived SFR for further analyses. We measure the SSFR for this galaxy to determine if the star formation rate is similar to that for a typical star forming galaxy. We calculate the stellar mass in the same manner described above. This galaxy has a *K*-band magnitude of 9.94 (Devereux et al. 2009) and a *B* – *V* colour of 0.59 (Schroeder & Visvanathan 1996), which yields a stellar mass-to-light ratio of 0.75 and a stellar mass of $4.4 \times 10^9 M_{\odot}$. This corresponds to a log(SSFR) of -10.6. This galaxy falls below the typical range of field SSFR values for its stellar mass (Tyler et al. 2013). This may indicate that its SFR has been suppressed through environmental processes, but it is worth noting that its SFR is not significantly lower than the observed range of typical SFR values for field galaxies. All evidence suggests that the galaxy has already experienced significant ram-pressure stripping. It is likely that this galaxy has already passed through the densest part of the ICM and is on its way out. This hypothesis is investigated further in Section 4.1.

3.2.3. NGC 1427A

In terms of star formation and dust properties, NGC 1427A is the most unusual galaxy in our sample, as it is not a spiral galaxy but a dwarf irregular. Emission at 8 μm and 24 μm is clearly not as strong as in the other galaxies. A comparison of excess 8 μm and H α emission is particularly interesting. The *HST* H α image clearly shows emission confined to an arc, meaning that the majority of star formation is occurring within the arc. This was also confirmed by H α ground-based imaging by Georgiev et al. (2006). The excess 8 μm emission largely corroborates this view with a few significant differences. There appears to be 8 μm emission arranged in a line directly behind the head of the arc that is not clearly seen at H α . This may be due to a dust gradient within the galaxy that obscures part of the H α emission. Moreover, at the eastern edge of the galaxy, finger-like excess 8 μm emission is observed where the H α emission is mainly dominated by point sources. These star forming regions at 8 μm are a factor of 2 – 4 fainter than the other brighter regions that are located closer to the head of the arc. There is also a large gap spanning 2.5 kpc between the emission near the head of the galaxy and the eastern end of the galaxy, also observed at H α . A possible interpretation may be that the star forming knots seen on the eastern end of the galaxy are associated with

gas and dust that have been ram-pressure stripped, as evidenced by the wide gap between the two star forming regions and the finger-like $8 \mu\text{m}$ excess emission. The excess $8 \mu\text{m}$ image is also corroborated by the $24 \mu\text{m}$ image. Due to the poorer sensitivity of the $24 \mu\text{m}$ image, it only shows where significant star formation is occurring. It appears most of the star formation is confined to the southern side of the galaxy within the high IR flux extraction region, though some of the star formation in the eastern edge of the galaxy is also seen at $24 \mu\text{m}$.

We quantify the dust continuum emission from this galaxy by measuring the $24 \mu\text{m}$ emission within the galaxy extraction region and high IR flux extraction region and its star formation rate. Using the methods described earlier we determine the flux values of 12.9 ± 1.1 and 7.1 ± 0.6 mJy for the galaxy and high IR flux extraction regions, respectively. Because the high IR flux region is also located within galaxy extraction region, we conclude majority of the $24 \mu\text{m}$ flux ($\sim 60\%$) is confined to the high IR flux region. It is clear that the $24 \mu\text{m}$ luminosity of this galaxy is considerably fainter than the other three galaxies, meaning this galaxy harbors less warm dust than the other galaxies in the sample. We also calculate the stellar mass of this galaxy in order to place these results in context. The R and I -band magnitudes of 13.33 and 13.34, respectively, were measured by the HIPASS optical counterparts survey (Doyle et al. 2005). We use the Bell et al. (2003) $r' - i'$ mass-to-light ratio relation to estimate a stellar mass of $6.2 \times 10^8 M_{\odot}$, making it the lowest stellar mass object in our sample. An $H\alpha$ -derived star formation rate of $0.057 M_{\odot} \text{ yr}^{-1}$ is given by Georgiev et al. (2006). We convert this to a $H\alpha$ luminosity to derive our own $H\alpha / 24\mu\text{m}$ -based star formation rate using the Calzetti et al. (2010) relation. Assuming only foreground galactic extinction of the $H\alpha$ line and the $H\alpha$ -to-SFR relation used by Georgiev et al. (2006), we obtain an $H\alpha$ flux of $2.15 \times 10^{-13} \text{ erg s}^{-1}$ for the galaxy. This translates to a SFR of $0.065 M_{\odot} \text{ yr}^{-1}$, which is consistent with the value derived by Georgiev et al. (2006). This means that the $\log(\text{SSFR})$ for this galaxy is -10.0 . This value falls within the distribution for field galaxies and other star-forming galaxies in dense clusters (Tyler et al. 2013).

3.3. Fine Structure Lines

The fine-structure line flux ratios can be used to determine the excitation mechanism for the gas, and can provide clues about the hardness of the incident radiation field. Different excitation mechanisms produce different ionization ratios and therefore fine-structure lines emitted from photodissociation regions in galaxies can be used to delineate harder excitation sources (e.g. AGN) from softer ones (e.g. star formation). Dale et al. (2006) in their *Spitzer* IRS study of Seyfert, LINERS, HII nuclei, and extranuclear HII regions found that they could isolate each type of source in a $[\text{NeIII}] 15.56 \mu\text{m}/[\text{NeII}] 12.81 \mu\text{m}$ and $[\text{SIII}] 33.48 \mu\text{m}/[\text{SiII}] 34.82 \mu\text{m}$ space. We carry out a similar analysis to see if there are any unusual signatures in our derived fine structure line fluxes, which may either be associated with a shock or excitation by the hard cluster X-ray radiation field. For example, if the main excitation mechanism of the gas is X-ray irradiation from the intracluster medium, one might expect

more AGN-like line ratios. The fine structure line ratios for the spectral extraction regions for all of our galaxies are shown in Figure 19.

We find that the ionization state of the gas for three of our sample galaxies, 97073, NGC 4522, and ESO 137-001, falls within the star-forming region locus of the $[\text{NeIII}]/[\text{NeII}]$ versus $[\text{SIII}]/[\text{SiII}]$ plot. However, NGC 1427A shows rather unusual ionization state that is similar to Seyferts and LINERS, which may be due to its close proximity to the center of Fornax clusters X-ray emission. In galaxies where we see excess warm H_2 emission (i.e. 97073, NGC 4522, and ESO 137-001), we do not see any unusual fine-structure line ratios; there is no indication that these lines are excited by the hard X-ray emission within the cluster even in the tail regions of these galaxies. In these cases, the observed lines are most likely emitted within PDRs associated with star forming regions and not associated with the unusually excited molecular hydrogen.

The unusual $[\text{SIII}] 33.5\mu\text{m}/[\text{SiII}] 34.8\mu\text{m}$ line ratio observed in NGC 1427A could be entirely due to the faintness of the $[\text{SIII}] 33.5 \mu\text{m}$ line. One way to determine if the line flux is peculiar is to compare it to a higher excitation line of the same species, the $18.7 \mu\text{m}$ $[\text{SIII}]$ line. The typical $[\text{SIII}] 18.7 \mu\text{m}$ -to- $[\text{SIII}] 33.5\mu\text{m}$ ratio for the SINGS sample is 0.82 with a standard deviation of 0.27 (Dale et al. 2006). In the case of NGC1427A, the ratio is much higher (> 2). It is also worth noting that the $[\text{SIII}] 18.7 \mu\text{m}$ emission is not centered on, but is slightly offset inward from, the brightest star forming region. This suggests that the faintness of the $[\text{SIII}] 33.5 \mu\text{m}$ is likely real and is not likely a signal-to-noise issue. This could be potentially explained by two different effects: a hard UV radiation field and/or increased electron densities. While the former seems likely due to galaxy's proximity to the center of Fornax where the density of the hot ICM is the greatest, one can compare the $[\text{NeIII}]/[\text{NeII}]$ ratio, which is a good indicator of hardness of radiation, with galaxies with known hard UV fields such as blue compact dwarfs (BCDs). For a select sample of low metallicity BCDs, Wu et al. (2008) find typical ratios of $\sim 3 - 5$, which is consistent with the lower limit set by our measurements. The lower $[\text{SIII}]/[\text{SiII}]$ ratio can also be explained by increased electron densities. A ratio of > 2 is consistent with densities $> 10^3 \text{ cm}^{-3}$ (Rubin 1989). This galaxy already exhibits significant compression through ram-pressure, which could lead to the enhanced densities. Based on the available information, it is not possible to distinguish between these two scenarios.

The blended feature of $[\text{OIV}] 25.9\mu\text{m}$ and $[\text{FeII}] 26.0\mu\text{m}$ has been detected in most spectra with the exception of those from NGC1427A. The weakness of the higher ionization $[\text{NeIII}] 15.6\mu\text{m}$ line makes $[\text{FeII}]$ the most likely line detected in the blended feature. As discussed in Cluver et al. (2010), the $[\text{SiII}]/[\text{NeII}]$ and the $[\text{FeII}]/[\text{NeII}]$ line ratios can be used as a diagnostic for shocks. For our sample, typical values of $[\text{SiII}]/[\text{NeII}]$ fall within a narrow range of 0.87 to 1.35 whereas the $[\text{FeII}]/[\text{NeII}]$ ratio ranges from 0.05 to 0.20, which are similar to values observed by Cluver et al. (2010). Typical SINGS galaxies that are not experiencing ram-pressure stripping have $[\text{FeII}]/[\text{NeII}]$ ratios lower than 0.05 (Wong et al. 2014). Although the elevated values suggest the presence of shocks, they can-

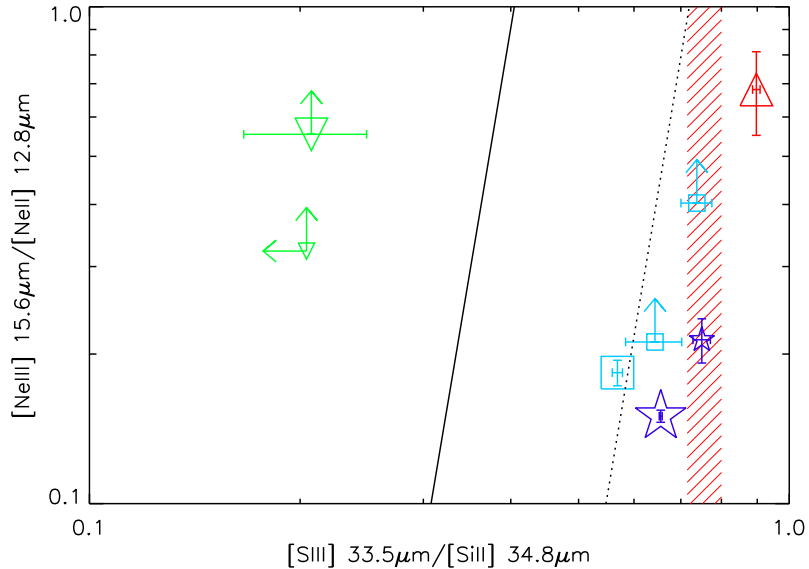


FIG. 19.— Neon, sulphur, silicon fine structure line diagnostic diagram. The line ratios of these lines indicate the ionization state of the gas. The solid and dashed lines separate regions with ionization states of gas in different classes of galaxies (see Dale et al. (2006) for more information). Gas in Seyfert galaxies and LINERS generally falls in the region to the left of the dashed line, while gas in star forming galaxies and regions generally falls to the right of that line. There are no star forming regions found to the left of the solid line. We show the line ratio for the different regions of our galaxy sample. The red triangular point represents the values obtained from our analysis of 97073. The large symbol represents the full galaxy extraction region while the red cross-hatched box represents the allowable values for the tail extraction region because neither neon line was detected. The blue square points represent the two extraction regions in NGC 4522. The large symbol represents the nuclear region of NGC 4522 while the smaller symbols represent the two regions where ram-pressure is thought to be stripping gas. The green upside down triangles represent the extraction regions in NGC1427A. The larger symbol represents the large extraction region while the smaller one represents the smaller extraction region with most of the flux. We also include data for ESO 137-001 and its tail from Paper 1 in this figure with purple star symbols. The large star symbol designates the nuclear extraction region, while the smaller ones are from the H₂ tail with IRS SL/LL coverage. With the exception of NGC 1427A, all other regions show an ionization state that is consistent with star forming regions. The ionization state of the NGC 1427A gas suggests that its gas experiences a harder radiation field or is of a higher density due to ram-pressure compression.

not be explained entirely by either dissociative J-shock (Hollenbach & McKee 1989) or fast shock (Allen et al. 2008) models. J-shock models for density ranges of $10^3 - 10^4 \text{ cm}^{-3}$ for a broad range of velocities produce $[\text{SiII}]/[\text{FeII}] \sim 1$. Fast shock models on the other hand produce large $[\text{SiII}]/[\text{NeII}] \sim 10$ and $[\text{FeII}]/[\text{NeII}] \sim 1$ ratios (Cluver et al. 2010). A solution to this mismatch is the depletion of either Si and Fe through shocks, which has been posited by both Cluver et al. (2010) and Wong et al. (2014).

4. DISCUSSION

The goal of our study was to test the hypothesis that warm H₂ emission can be produced through an interaction between the ICM and an infalling galaxy’s ISM, and that this emission can be used as an effective tracer of ram-pressure stripped gas. Consequently, galaxies showing strong signs of on-going ram-pressure stripping were chosen for this survey. Warm H₂ emission was detected in all four galaxies at varying degrees of strength and in some cases it was seen well outside the galaxy. In this section, we ascertain the impact on the star forming properties of galaxies due to ram-pressure, determine if the H₂ emission is anomalous and if so determine its excitation mechanisms, and how effective it may be in tracing on-going ram-pressure stripping.

4.1. The Impact on Star Formation due to Ram-pressure Stripping

To determine the effects of ram-pressure on the star formation, we place our measurements of the star forming properties of the galaxies in a broader context by comparing with other studies of cluster and field galaxies. It is clear that ram-pressure is having a significant effect on the star forming properties of the galaxies simply from the observed morphological differences compared to undisturbed galaxies, such as displaced dust disks, H α trails, and arc-like star-forming regions. To test whether the overall star-forming rates are also affected by ram pressure, we compare to measurements of other field galaxy samples. We present the specific star formation rates as a function of stellar mass in Figure 20 for all four galaxies in our sample using H α and 24 μm measurements to estimate the SFR and stellar mass, which were presented in Section 3.2.

In order to determine if ram-pressure stripping has significantly impacted these galaxies, we compare their SSFRs with typical values for field galaxies. While many measurements of the field galaxy star formation rates exist, we compare with Tyler et al. (2013) measurements due to the similarity of their methods with ours. Tyler et al. (2013) also employ H α and 24 μm flux measurements of galaxies to determine SFRs, and use these to estimate the typical star formation rates of local field galaxies as a function of their stellar mass. We present our results of the comparison in Figure 20 where it is seen that three out of four of our galaxies, 97073, NGC 1427A, and ESO 137-001, lie within the 1σ spread of star for-

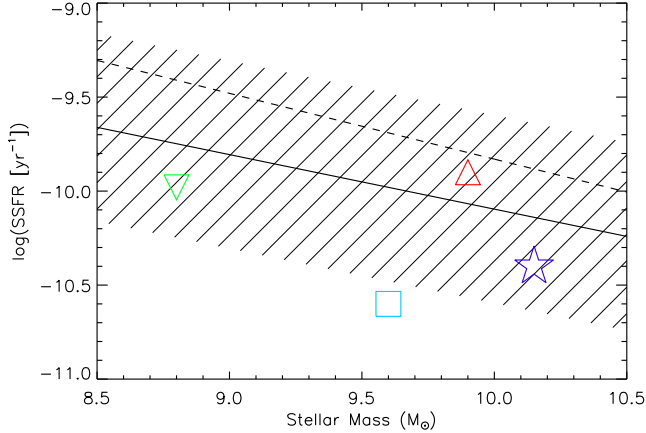


FIG. 20.— Specific star formation rate as a function of galaxy stellar mass. The red triangle, blue square, green upside down triangle, and purple star represent 97073, NGC 4522, NGC 1427A, and ESO 137-001, respectively. The solid line is the mode of the specific star formation rate obtained from Tyler et al. (2013) for field galaxies, while the hashed region represents the 1σ spread in the values. Three out of four of our galaxies fall within the typical values observed by Tyler et al. (2013). NGC 4522 shows signs of suppression. The dashed line is a similar relation obtained from Salim et al. (2007) where the star formation rate was measured using UV data using galaxies dominated purely by star formation with no AGN contribution. The offset between the Salim et al. (2007) and Tyler et al. (2013) could be explained from systematics arising from the different measurement techniques.

mation values of typical field galaxies. The four galaxies in our sample are, as an ensemble, consistent with being drawn from the field distribution (i.e., one galaxy, NGC 4522, just beyond $1\text{-}\sigma$ is expected and seen). For reference, we also compare with other star formation studies of field galaxies that have been done with UV and/or $H\alpha$ measurements (e.g. Brinchmann et al. 2004; Salim et al. 2007). UV and $H\alpha$ measurements, which often rely on an accurate determination of extinction and the intrinsic UV colors of the underlying stellar population, are not directly sensitive to heavily obscured star formation which can significantly impact estimates of SFR. This can yield significant systematic offsets in SFR measurements obtained using different methods as seen in Figure 20 where the Salim et al. (2007) relation is also plotted (see Boquien et al. (2012) and Elbaz et al. (2007) for more details). However, using both $H\alpha$ and $24\mu\text{m}$ measurements directly accounts for both unobscured and obscured star formation as we have done in our case. In conclusion, 97073, NGC 1427A, and ESO 137-001 show signs of healthy star formation, while NGC 4522 shows, at most, a small amount of suppression.

This means that ram-pressure has not significantly altered the star forming rates of these galaxies. However, there is an added possibility that ram-pressure induced star formation may compensate for any overall global reduction in star formation, as some galaxies show signs of ram-pressure enhanced star formation on the windward side of the galaxy. There is evidence observed in Virgo galaxies, including NGC 4522, that there is an enhancement in the molecular gas fraction and a possible increase of the star formation efficiency in the windward side of the galaxies (Vollmer et al. 2012), which together might enhance the star formation rate. However in this same work, there are signs that stripped gas, having lost the

gravitational confinement of the disk, can have lower star formation efficiency. Vollmer et al. (2012) explain that without the gravitational potential of the disk, shocks, as observed in this work, can increase the thermal and turbulent pressure of the gas and significantly decrease its star formation efficiency as it disperses when blown out of the galaxy. This might explain why even though we observe warm H_2 emission where molecular gas has been stripped, we do not see a commensurate increase in star formation activity in those regions.

4.2. Comparison with SINGS Galaxies

H_2 is typically excited within photodissociation regions through UV fluorescence in star forming regions. This explains most of the warm H_2 emission detected in the nearby SINGS galaxy sample (Roussel et al. 2007), which we use as a reference. However, our goal is to detect anomalous H_2 excitation that is likely associated with ram-pressure stripping. Unfortunately, it is impossible to determine the source of H_2 excitation from just the lowest ground state rotational transition line ratios because they have low enough critical densities that they are typically thermalized (Roussel et al. 2007). To disentangle the excitation mechanism for the H_2 emission, we use two different metrics that use additional information to determine if the H_2 emission is anomalously higher than what is produced by just star formation.

The first metric, presented in Paper 1, is the ratio of *MIPS* $24\mu\text{m}$ flux, a proxy for star formation, and the sum of the line fluxes of the ground-state rotational H_2 lines S(0) thru S(3), a proxy for total H_2 line emission. We apply our metric to all of the SINGS galaxies in the Roussel et al. (2007) sample and show the results in Figure 21. The error bars shown only include the error in the H_2 line fluxes and not the $24\mu\text{m}$ fluxes because $24\mu\text{m}$ fluxes typically have very small errors. Almost all of the galaxies have a ratio of less than 0.03, which we define as the threshold for anomalous H_2 emission. Roussel et al. (2007) highlight NGC 4450 and NGC 4579, two galaxies that are significant outliers in this relation, because their H_2 excitation cannot be explained by star formation or supernova remnants alone. They evoke either X-ray irradiation or shocks through cloud collisions as a possible explanation for the anomalous values.

We calculate the values for the metric for all of our galaxies and plot the values in Figure 21. H_2 fluxes are obtained from line fits of the extraction regions explored in this paper and Paper 1. If the detections of the S(1), S(2), and/or S(3) lines are not significant, we do not include them in the H_2 line flux sum. The error bars show both the errors in the $24\mu\text{m}$ fluxes and the root-sum-squared flux for the ratio that includes both the error in the H_2 line flux and the $24\mu\text{m}$ flux. The values obtained from regions that represent the galaxies as a whole are plotted with larger symbols, while the other regions of interest are plotted with smaller symbols. The individual symbols for each galaxy are explained in the figure captions. It is clear that for 97073, ESO137-001, and NGC4522 the extraction regions where stripping is occurring or one sees a tail have metric values that are outliers and therefore have significantly enhanced warm H_2 emission that cannot be explained simply by star formation. The tail region of 97073, represented by the small red triangular symbol, is definitely an extreme example as

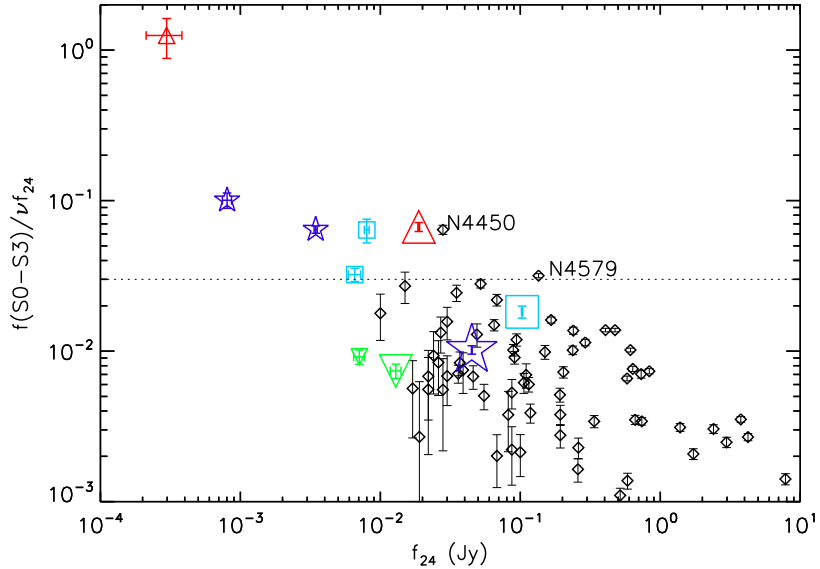


FIG. 21.— Comparison of ground state rotational H₂ line flux (S(0) thru S(3) transitions) to 24 μm flux as a function of 24 μm flux for the galaxies investigated in our IRS sample. In some cases where there were no detections of the S(1), S(2) and/or S(3) lines, only the detected lines are included in the H₂ flux. The open diamond points are galaxies from the SINGS sample with warm H₂ detections (Roussel et al. 2007). The significant outliers in Roussel et al. (2007)’s sample, NGC 4450 and 4579, are marked in the figure. The warm H₂ in these galaxies is thought to be heated by shocks or X-ray irradiation, as the H₂ line fluxes cannot be adequately explained by star formation or supernova remnants. The red triangular point represents the values obtained from our analysis of 97073. The large symbol represents the full galaxy extraction region while the smaller symbol represents the tail extraction region. The blue square points represent the two extraction regions in NGC 4522. The larger symbol represents the nuclear region of NGC 4522 while the smaller symbols represent the two regions where ram-pressure is thought to be stripping gas. The green upside down triangles represent the extraction regions in NGC1427A. The larger symbol represents the large extraction region while the smaller one represents the smaller extraction region with most of the flux. We also include data for ESO 137-001 and its tail from Paper 1 in this figure with purple star symbols. The large star symbol designates the nuclear extraction region, while the smaller ones are from the H₂ tail. The one with the lower flux ratio is the Tail (SL/LL) region, while the larger value is from the Far Tail (LL-only) region. In Paper 1, we showed that the warm H₂ tail in ESO 137-001 was not excited solely by star formation. This figure confirms that the warm H₂ observed in 97073 and the ram-pressure stripped regions of NGC 4522 are not heated solely by star formation and must have some other excitation mechanism. The tail region of 97073 is particularly striking as it has a ratio that is at least an order of magnitude higher than the regions in any other galaxy.

it has significantly more warm H₂ excess emission than any other galaxy in the sample. In fact, the offset H₂ emission seen in 97073 strongly suggests that H₂ is being dissociated from the head of the galaxy where significant star formation is occurring and reforming some distance behind the area of intense star formation in an excited state. Furthermore, a significant fraction of its H₂ mass is in the warm state. In terms of anomalous metric values, the far tail region of ESO 137-001 comes in as a distant second, followed by the SW region of NGC 4522. If one looks at metric values for the galactic extraction regions themselves, ESO 137-001 and NGC 4522 fall within the normal values representative of star forming galaxies in the SINGS sample. 97073, on the other hand, has enhanced emission even within the galaxy. NGC 1427A does not have any enhanced H₂ emission within either the galaxy or the high IR flux regions. In fact, it has the lowest values of the metric compared to all other galaxies and exhibits unusual H₂ emission characteristics where only the lowest energy rotational line S(0) is detected.

The second metric more directly tracks star formation powered photodissociation regions (PDR) as being the location of the warm H₂ emission. In recent work of galaxies with anomalous H₂ emission, the H₂ line flux versus 7.7 μm PAH flux ratio has been an excellent discriminator of anomalous H₂ emission (Appleton et al. 2006; Roussel et al. 2007; Ogle et al. 2010; Guillard et al. 2012b). Ogle et al. (2010) empir-

ically show through a comparison of SINGS galaxies that their molecular hydrogen emission galaxies (MOHEGs) are powered either by shocks or cosmic rays because their H₂-PAH flux ratios fall in the 0.04 – 4 range. Guillard et al. (2012b), in Figure 7 of their work, show the large range of galaxies with anomalous H₂ emission and confirm that star formation powered H₂ emission cannot explain flux ratios greater than 0.04. They further support this claim by running PDR models using existing code (Le Petit et al. 2006), which were found to be consistent with other models of H₂ emission in PDRs (Kaufman et al. 2006). We present the flux comparison for our measurements in Figure 22. It is worth noting that the far tail region of ESO 137-001 where this ratio would be the highest in that system is not included due to the lack of short wavelength IRS coverage. We also plot the ratios for star forming SINGS galaxies using the 7.9 μm and H₂ line flux measurements carried out by Roussel et al. (2007). It is clear that the star forming SINGS galaxies form a narrow band in H₂/PAH flux ratio with typical values slightly less than 0.01. The results of our measurement are consistent with our conclusions from the use of our first metric. The regions that are experiencing stripping all fall above the 0.04 flux ratio cut with the exception of NGC1427A, which is thought not to be experiencing significant stripping. 97073 remains the most dramatic example falling well above the relation with almost 60 times the flux ratio of star forming SINGS

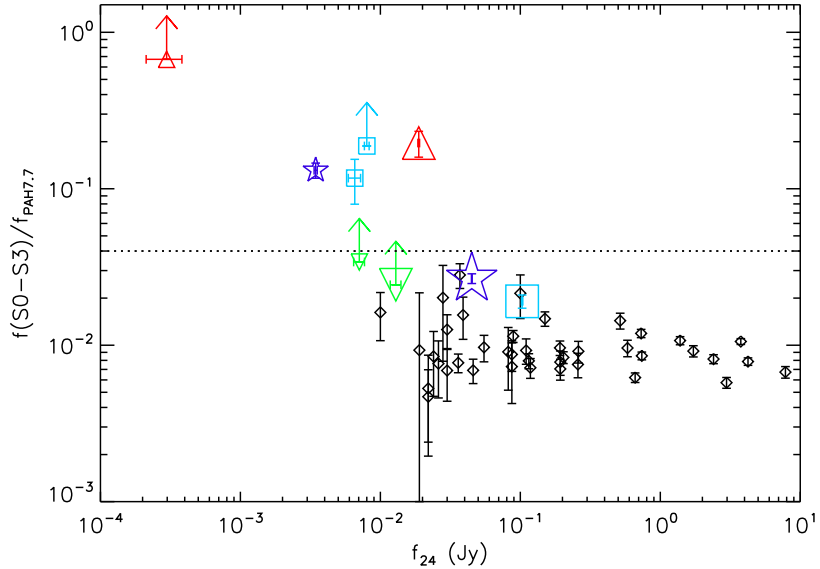


FIG. 22.— Comparison of ground state rotational H_2 line flux (S(0) thru S(3) transitions) to $7.7 \mu\text{m}$ PAH feature flux as a function of $24 \mu\text{m}$ flux for the galaxies investigated in our IRS sample. In some cases where there were no detections of the S(1), S(2) and/or S(3) lines, only the detected lines are included in the H_2 flux. The symbols are the same as those used in Figure 21. The Far Tail region in ESO 137-001 was not included because the IRS spectrum does not cover shorter wavelengths that included the $7.7 \mu\text{m}$ PAH feature. The open diamond points are values obtained for star forming regions from SINGS galaxies from Roussel et al. (2007). The SINGS points have an average H_2 to PAH ratio of ~ 0.01 . The dotted line represents the maximum ratio that can be explained by PDRs within normal star-forming galaxies and dwarfs (Ogle et al. 2010; Guillard et al. 2012a). Larger ratios are most likely explained by shock excitation of H_2 .

galaxies. NGC 4522 shows modestly elevated flux ratios with almost 10 times the SINGS average. This is slightly higher than similar measurements made by Wong et al. (2014) of the same galaxy where they find an increase of 3–5 times of the SINGS average. The difference may be attributed to different extraction regions and our inclusion of the S(3) to the H_2 flux measurement. Nevertheless, two conclusions can be drawn from this comparison: (1) star formation itself is insufficient for exciting the H_2 and (2) We observe a sequence of galaxies with varying levels of H_2 excitation, which may be due to the current evolutionary state of the galaxy; this is discussed further below.

4.3. The Source of Warm H_2 Excitation

As discussed in the introduction, a number of potential excitation mechanisms for H_2 beyond star formation were reviewed. To get a better understanding of potential excitation mechanisms, we can estimate the timescale of warm H_2 emission if there was no *in-situ* energy source. Using the ideal gas law for a diatomic molecule, the time scale τ can be approximated to be

$$\tau \sim \frac{5}{2} N_{H_2} k T_{H_2} / L_{H_2} \quad (2)$$

where N , T , and L are the number, temperature, and luminosity of H_2 molecules, respectively. For our estimation, we only consider the warm component of the H_2 since it has been characterized in the tail regions of all three galaxies with anomalously high H_2 emission. We take L_{H_2} to be the sum of the luminosities of the S(0) and S(1) lines. We obtain an L_{H_2} of $3.2 \times 10^6 L_\odot$, $5.6 \times 10^6 L_\odot$, and $4.6 \times 10^5 L_\odot$ for the Full Tail region of ESO137-001, the Tail region of CGCG97-073, and both

the NE and SW tail regions of NGC4522, respectively. The timescales of these regions correspond to 4, 8, and 8 kyr. One can also estimate the true time scale of the H_2 emitting regions if the geometry of a galaxy’s orbit and its velocities are known. ESO 137-001 is the best candidate for this measurement as its orbit is along the plane of the sky. Taking a conservative galaxy velocity of 1600 km s^{-1} and a tail length of 20 kpc (Sivanandam et al. 2010), we obtain a time scale of its H_2 tail of 12 Myrs. A similar estimation of NGC4522 can be made, but its orbit is not along the plane of the sky. With its projected tail length of 4kpc and a galaxy velocity estimate of 1000 km s^{-1} along the plane of the sky, we obtain a timescale of 4 Myrs. It is clear from our sample that the true timescales of these warm H_2 tails are much longer than the radiative timescales of the warm gas. This means that there must an *in-situ* source of energy that continuously heats the gas.

Of the several potential excitation sources such as MHD waves, conduction, cosmic ray heating, and X-ray dissociation regions (XDRs), shock excitation seems to be the most likely explanation. We can make a morphological argument to support this view. In most cases, it is clear that the central regions of these galaxies do not show anomalous H_2 -PAH flux ratio whereas their stripped H_2 trails show significant enhancement of H_2 emission. This is especially seen in 97073 in Figure 7 where there is a clear offset between the regions with significant star formation where H_2 does exist and those where warm H_2 is observed. The cluster centric sources such as MHD waves and cosmic ray heating should not discriminate where in the galaxy they deposit their energy. Moreover, these processes generally yield hotter ($T \sim 300\text{K}$; Johnstone et al. (2007)) H_2 temperatures.

For similar reasons, conduction and XDRs cannot adequately explain the morphology. Of course, if the observed excitation is indeed due to turbulent shocks, which are induced by ram-pressure stripping, there needs to be sufficient kinetic energy dissipated to account for the observed H₂ luminosity.

To calculate the amount of energy extracted from the ram-pressure stripping process, we present a toy model to estimate the loss in kinetic energy of the galaxy from ram-pressure drag as it falls into a galaxy cluster. This energy would then be injected into the stripped ISM of the galaxy and the ICM either through turbulent or viscous processes as the galaxy travels through the cluster (see Roediger & Brüggen (2008) for a discussion). Ram-pressure, P_{ram} , introduces a drag force that decelerates the galaxy:

$$a_{drag} = -\frac{P_{ram} A_{ISM}}{M_{gal}} \quad (3)$$

$$= -\frac{\rho_{ICM} v_{gal}^2 A_{ISM}}{M_{gal}} \quad (4)$$

where a_{drag} is the deceleration experienced by the galaxy, A_{ISM} is the galaxy ISM's cross-sectional area, M_{gal} is the mass of the galaxy, v_{gal} is its orbital velocity, and finally, ρ_{ICM} is the density of the ICM at the galaxy position. If we assume the ram-pressure is not changing in relative short time scales and that the galaxy is traveling face-on to the ICM wind, we can make the following simplification to determine loss of kinetic energy:

$$\frac{dE}{dt} = \frac{d}{dt}(M_{gal} a_{drag} s) \quad (5)$$

$$= M_{gal} a_{drag} \frac{ds}{dt} \quad (6)$$

$$= -P_{ram} A_{ISM} v_{gal} \quad (7)$$

$$= -\rho_{ICM} v_{gal}^3 A_{ISM} \quad (8)$$

where s is the distance traveled by the galaxy. The above equation can be written in more convenient units below:

$$\frac{dE}{dt} = -7.8 \times 10^8 \left(\frac{\rho_{ICM}}{10^{-27} g cm^{-3}} \right) \times \left(\frac{v_{gal}}{1000 km s^{-1}} \right)^3 \left(\frac{r_{gal,ISM}}{10 kpc} \right)^2 L_{\odot} \quad (9)$$

A few observations can be made from this derivation. First, the energy loss is the strongest as an infalling galaxy approaches the cluster core where the ICM density is the highest and the infalling galaxy is traveling the fastest. Second, as the ISM of the galaxy is stripped away, the cross-sectional area decreases thereby reducing the kinetic energy loss. We calculate the expected kinetic energy loss rate for the three galaxies with anomalous H₂ emission. The calculated energy loss rate for ESO 137-001 with values obtained from Paper 1, $\rho_{ICM} = 2.2 \times 10^{-27} g cm^{-3}$, $v_{gal} = 1602 km s^{-1}$, and $r_{gal,ISM} = 3 kpc$, is $6.4 \times 10^8 L_{\odot}$. This is a few orders of magnitude more than the observed H₂ luminosity. Moreover, this galaxy has an observed X-ray (Sun et al. 2006, 2010) and H α (Sun et al. 2007) tails with combined luminosity in the $10^7 L_{\odot}$ range. The combined

power output of these tails is consistent with the maximum power produced by the dissipation of the galaxy's kinetic energy through ram-pressure stripping. A similar calculation for NGC 4522 for a parameter choice of $\rho_{ICM} = 10^{-28} g cm^{-3}$, $v_{gal} = 1500 km s^{-1}$ (Kenney et al. 2004), and $r_{gal,ISM} = 2.4 kpc$ (estimated from the $8\mu m$ image) yields a energy loss of $1.5 \times 10^7 L_{\odot}$. Finally for 97073, the calculated energy loss rate is $1.2 \times 10^9 L_{\odot}$. For this galaxy, ρ_{ICM} of $1.1 \times 10^{-27} g cm^{-3}$ was obtained from Mohr et al. (1999) and v_{gal} was estimated to be $\sqrt{3}\sigma$ where σ , the cluster velocity dispersion, was $891 km s^{-1}$ (Cortese et al. 2004). $r_{gal,ISM}$ was estimated to be 6.1 kpc from the $8\mu m$ image. All of the observed H₂ luminosities can be explained by the energy loss by the ram-pressure drag experienced by the galaxy. What is also particularly interesting is that the calculated energy loss rate seems to track the magnitude of anomalous warm H₂ emission discussed in the previous section. This may be additional evidence for the dissipation of kinetic energy being the source of energy for the observed emission.

4.4. Tracing Ram-Pressure Stripping with Warm H₂ Emission

We place the results of our survey in a general context by attempting to answer the question of how excess warm H₂ emission relates to ram-pressure stripping. As discussed in Section 4.2, three of the four galaxies show enhanced H₂ emission and all three of them show evidence for a warm H₂ tail, while two of them, ESO 137-001 and NGC 4522, show strong evidence for extraplanar star formation. The fourth galaxy shows signs of ram-pressure induced star formation but no enhanced warm H₂ emission or tail. If one arranges all galaxies in ascending order of their total gas mass, assuming ESO 137-001 has a HI mass close to the measured upper limit of $1 \times 10^9 M_{\odot}$ (Sun et al. 2007), we would have NGC 4522 with the least mass, followed by ESO 137-001, 97073, and NGC 1427A. In descending order of projected distance from their respective cluster centers we have: NGC 4522, 97073, ESO 137-001, and NGC 1427A.

This suggests a possible evolutionary sequence as an explanation for the observed differences in the properties of the four different galaxies. The first stage is represented by NGC 1427A. NGC 1427A is likely at the initial stages of being stripped by ram-pressure where the ICM does not have significant strength to strip out the molecular and HI gas, as evidenced by the extremely large HI mass measurement for this galaxy (Koribalski et al. 2004). This is plausible because, even though NGC 1427A is very close to the center of the Fornax cluster (only 130 kpc in projected separation), the cluster is very poor and has a fairly low ICM temperature of 1.6 keV (Ikebe et al. 2002). Furthermore, this galaxy has a large recession velocity with respect to the cluster mean ($\sim 650 km s^{-1}$), and it is also possible that its actual radial separation from the cluster core may be much larger than what is observed. This galaxy was originally chosen to be part of the sample due to its prominent arc-like star forming regions (Georgiev et al. 2006). It also has an unusually large atomic gas reservoir. The galaxy is most likely experiencing some ram-pressure, which is able to induce star formation by compressing gas to form stars

where the ram-pressure is significant, but the pressure is not high enough to remove molecular gas or excite H_2 through the interaction.

The second stage is likely represented by 97073 where the interaction between the ICM and the galaxy's ISM becomes strong enough to dissociate the molecular gas and reform it in an excited state downstream, possibly through shocks, in addition to inducing star formation along the leading edge of the galaxy. 97073 is in a moderately rich cluster that has a relatively hot ICM with a temperature of 3.6 keV (Ikebe et al. 2002). The images of the galaxy at $\text{H}\alpha$, and 8 μm clearly show an arc of star formation occurring at the location directly opposite to the $\text{H}\alpha$ tail. The 24 μm image also shows intense dust continuum emission that coincides with the star forming arc. Furthermore, this galaxy's tail region exhibits the strongest warm H_2 excess of all the regions explored, while the galaxy itself exhibits an excess that is stronger than all other galactic regions considered. It is very likely that this galaxy is just beginning to experience strong ram-pressure. Its excess 8 μm emission is not truncated in any way, which suggests that there is sufficient molecular gas throughout the galaxy to promote star formation. It has a healthy amount of gas, both in molecular and atomic form, and it has a healthy star formation rate. The current rate of stripping cannot be as significant as ESO 137-001 because we do not see large star forming knots trailing behind the galaxy. Unfortunately, due to the alignment of the IRS slit, the true length of the warm H_2 tail was not determined.

The third stage is probably represented by ESO 137-001 where a significant fraction of atomic and molecular gas has been stripped from the galaxy and a significant fraction of molecular gas is within the observed $\text{H}\alpha$ and X-ray tails as discussed in Paper 1. This galaxy is also fairly close in projected separation (~ 280 kpc) to the core of Abell 3627, which is the hottest cluster in our sample with an ICM temperature of 6 keV (Sun et al. 2006). The galaxy has an upper limit on its HI mass of $10^9 M_\odot$ (Sun et al. 2007) and no published values for its cold molecular gas content. The galaxy still has a relatively healthy star formation rate. It is clear from the 8 μm excess image that the emission is not as extended as the stellar disk and the galaxy has a trail of star forming knots stretching approximately 12 kpc from the galaxy center. This trail of star forming knots is mostly embedded within the > 20 kpc long warm H_2 tail. The warm H_2 gas within the tail cannot be explained simply by star formation. The existence of long gaseous tails, the long trail of star forming regions, and truncated dust emission suggest that this galaxy may be further along in its ram-pressure stripping phase than the previous two galaxies.

NGC 4522 possibly represents the last stage of this process. Observational signatures show this galaxy to be similar to ESO 137-001 in many ways. It has a smaller dust disk than its stellar disk. It has extraplanar dust emission albeit at a smaller scale, and similarly a ~ 4 kpc long H_2 tail, which has a factor of 5 – 10 less mass than the H_2 tail in ESO 137-001. This galaxy is also fairly poor in gas, with comparable HI and molecular gas content, and the HI gas is known to be displaced in the direction of stripping (Kenney et al. 2004). All signs sug-

gest that this galaxy is either in a similar phase to ESO 137-001 but is less affected by ram-pressure because this galaxy is in a much cooler cluster and not as dense a region of the ICM, or in a later phase where ram-pressure is becoming less significant. The morphologies of its dust and H_2 trails also suggest that it is on its way out of the cluster core. Vollmer et al. (2006) suggest from their dynamical modeling of VLA HI data that this galaxy must have passed through peak ram-pressure stripping 50 Myrs ago. Spectroscopic observations corroborate this finding where a K+A spectrum is seen in the outer stellar disk of the galaxy. Stellar population modelling suggests that the star formation in the outer stellar disk was quenched ~ 100 Myr ago (Crowl & Kenney 2006). This most likely explains the suppressed star formation observed in this galaxy. This galaxy has a few peculiarities as it is approximately 1 Mpc away from Virgo's center and the traditional view is that ICM cannot be dense enough to ram-pressure strip the galaxy significantly in a fairly low temperature cluster (~ 2.4 keV; White 2000) at that distance assuming a typical velocity for a galaxy, as discussed above. But in this case, the galaxy has a fairly large recessional velocity with respect to the cluster mean ($\sim 1000 \text{ km s}^{-1}$). While it is clear from the multiple observational signatures that the galaxy is experiencing ram-pressure stripping, this may require that the ICM be dynamic, i.e. it is moving relative to the cluster mean, and its density is enhanced, or the galaxy is traveling at very high speeds and is unbound from the cluster (Vollmer et al. 2006).

Our study shows that warm H_2 heated by the interaction between the ICM and ISM is not uncommon in cluster galaxies experiencing significant ram-pressure stripping. In the most extreme cases of warm H_2 emission, i.e. ESO 137-001 and 97073, there are long 40 – 70 kpc tails observed at other wavelengths. There may be a strong association between the existence of an extra planar star formation/ $\text{H}\alpha$ emission and a warm H_2 tail. However, a greater number of detections of H_2 tails is required to confirm this association. If one assumes such an association is true, the recent discovery of more than a dozen galaxies in Coma with extended $\text{H}\alpha$ knots (Yagi et al. 2010) and UV trails (Smith et al. 2010) may suggest that warm H_2 tails may be present in all galaxies with significant ram-pressure stripping, and may be an indicator of direct stripping of molecular gas.

5. CONCLUSIONS

We present the results of a study of four galaxies, known to be currently undergoing ram-pressure stripping, to detect shock-heated warm H_2 emission associated with galaxies' interaction with the ICM. The results for one of our galaxies, ESO 137-001, have already been published in Paper 1. The main results of our study are as follows:

1. We detect warm H_2 emission in all four galaxies within the sample. The ground state rotational H_2 S(0) line is observed in all four of galaxies. The S(1), S(2), and S(3) lines are detected in ESO 137-001, CGCG 97-073, and NGC 4522. Warm H_2 emission is also detected in extraplanar regions of ESO 137-001, CGCG 97-073, and NGC 4522 indicating that molecular gas is present in ram-pressure stripped gas. ESO 137-001 exhibits a warm H_2 tail > 20 kpc in length, while NGC 4522 has

one that is ~ 4 kpc in length. Even though a portion of the tail was observed in CGCG 97-073, the length of this galaxy's warm H₂ tail could not be ascertained. NGC 1427A exhibited no signs of a H₂ tail, but had strong H₂ emission associated with the brightest star-forming regions located on the southern edge of the galaxy.

2. We measure the thermodynamic properties of the warm H₂ gas, such as temperature, column density, and total mass, in all four galaxies both within the galaxies themselves and also in other regions of interest likely associated with ram-pressure stripping. We find similar temperature distributions in ESO 137-001, CGCG 97-073, and NGC 4522. The H₂ emission could be adequately fit by a two-temperature model, one warm (T= 115 – 160K) and the other hot (T= 400 – 600K). In the case of NGC 1427A, we were only able to place an upper limit on its gas temperature of T= 90 – 105K due to the lack of detection of the S(1) line. This anomaly could be explained by either a lower than expected ortho-to-para ratio and/or unusually cool H₂ gas. The column densities of the warm H₂ gas within the explored regions vary somewhat but fall within the $10^{19} - 10^{20}$ cm⁻² range. The hot H₂ gas typically has densities that are two orders of magnitude less than the warm H₂, making the warm gas the dominant mass component. The detected total masses of warm H₂ amongst the explored regions within all four galaxies range from $10^6 - 10^8 M_{\odot}$, with CGCG 97-073 having the largest mass.

3. We observe clear signs of dust stripping in at least 2 out of 4 galaxies in our $8\mu\text{m}$ images in the form of extraplanar dust emission, which is also visible in the $24\mu\text{m}$ images. ESO 137-001 reveals emission by dust in a cometary morphology that is extended in the direction of the wind. In the case of NGC 4522 where we have the best spatial resolution, the turbulent nature of dust stripping is observed, as there are large knots and ripples in the stripped regions. It is possible that NGC 1427A may also be experiencing dust stripping as evidenced by long finger-like emission at $8\mu\text{m}$.

4. We study the star-forming morphologies of each of the galaxies and find signatures of ram-pressure induced arc-like star formation within the galaxy and/or extraplanar star formation from blown out gas. NGC 1427A is likely the most dramatic case of ram-pressure induced star formation within the galaxy, followed by CGCG 97-073, as both galaxies exhibit strong arc-shaped star forming regions. ESO 137-001 and NGC 4522 have extraplanar star forming regions that span 12 and 3 kpc, respectively.

5. We measure the star-forming rates in each galaxy within our sample to see if they are suppressed within the cluster environment. Three out of four galaxies, 97073, NGC 1427A, and ESO 137-001, fall within the typical star forming sequence for field galaxies, while NGC 4522

star formation rate falls slightly more than 1σ low.

6. We measure common fine structure lines and find that three out of four of our galaxies do not show unusual ionization states and they are generally consistent with star forming regions. However, the gas in NGC 1427A shows a very unusual ionization state that is similar to Seyferts and LINERs, which can be explained by higher electron densities or harder radiation field. The [FeII]/[NeII] ratio is elevated in our sample, suggesting potential shock excitation, but when combined with the [SiII]/[NeII] line ratio, the observed values are neither consistent with J-shock or fast shock models. This may be due to either Fe and/or Si depletion from shocks.

7. We compare the measured H₂ flux with the $24\mu\text{m}$ flux and $7.7\mu\text{m}$ PAH flux to determine if the H₂ emission is unusual in any way compared to a control sample consisting of SINGS galaxies with warm H₂ measurement. In three of our four galaxies, we observe excess H₂ emission, especially in regions where stripped gas is present. CGCG 97-073 is a special case where both the galaxy and the tail region are outliers, and its tail region is the most significant outlier of all the regions considered. NGC 1427A is the only galaxy without anomalously high H₂ emission.

8. There may be a possible association between extraplanar H α and H₂ emission because three of the four galaxies have coaligned H α and warm H₂ emission.

9. We hypothesize that excess warm H₂ emission may be a common feature of galaxies that are experiencing significant ram-pressure stripping and can be used as a tracer for this process. The varying degree of excess H₂ emission we have observed in our sample is most likely the result of galaxies at different stages of ram-pressure stripping (i.e. experiencing different levels of ram-pressure).

Lastly, when the *James Webb Space Telescope* is launched in the near future, the mid-infrared spectroscopic window will be opened again with the integral field spectrometer on the Mid-infrared Instrument. This will allow a much larger sample of galaxies to be investigated.

We thank Dr. Ming Sun and Dr. Lei Bai for their helpful suggestions. S. S. was supported by the Dunlap Fellowship at the University of Toronto. We thank the referee for their great suggestions to improve the paper. We also would like to thank the *Spitzer*/GTO team for support at the University of Arizona. This research has made use of the NASA/IPAC Extragalactic Database (NED) which is operated by the Jet Propulsion Laboratory, California Institute of Technology, under contract with the National Aeronautics and Space Administration. This research has made use of the GOLD Mine Database.

REFERENCES

- Allen, M. G., Groves, B. A., Dopita, M. A., Sutherland, R. S., & Kewley, L. J. 2008, ApJS, 178, 20
 Appleton, P. N., et al. 2006, ApJ, 639, L51
 Bai, L., Marcillac, D., Rieke, G. H., et al. 2007, ApJ, 664, 181
 Bell, E. F., McIntosh, D. H., Katz, N., & Weinberg, M. D. 2003, ApJS, 149, 289
 Bigiel, F., Leroy, A. K., Walter, F., et al. 2011, ApJ, 730, L13
 Blakeslee, J. P., Jordán, A., Mei, S., et al. 2009, ApJ, 694, 556
 Bloemen, J. B. G. M., Strong, A. W., Mayer-Hasselwander, H. A., et al. 1986, A&A, 154, 25
 Boquien, M., Buat, V., Boselli, A., et al. 2012, A&A, 539, A145
 Boselli, A., Gavazzi, G., Combes, F., Lequeux, J., & Casoli, F. 1994, A&A, 285, 69
 Boselli, A., & Gavazzi, G. 2006, PASP, 118, 517
 Brinchmann, J., Charlot, S., White, S. D. M., et al. 2004, MNRAS, 351, 1151
 Calzetti, D., et al. 2007, ApJ, 666, 870

- Calzetti, D., Wu, S.-Y., Hong, S., et al. 2010, *ApJ*, 714, 1256
- Chanamé, J., Infante, L., & Reisenegger, A. 2000, *ApJ*, 530, 96
- Cluver, M. E., et al. 2010, *ApJ*, 710, 248
- Corbelli, E., Bianchi, S., Cortese, L., et al. 2012, *A&A*, 542, A32
- Cortese, L., Gavazzi, G., Boselli, A., Iglesias-Paramo, J., & Carrasco, L. 2004, *A&A*, 425, 429
- Cortese, L., et al. 2007, *MNRAS*, 376, 157
- Cortese, L., Davies, J. I., Pohlen, M., et al. 2010, *A&A*, 518, L49
- Crowl, H. H., & Kenney, J. D. P. 2006, *ApJ*, 649, L75
- Dale, D. A., Smith, J. D. T., Armus, L., et al. 2006, *ApJ*, 646, 161
- Davies, J. I., Bianchi, S., Cortese, L., et al. 2012, *MNRAS*, 419, 3505
- Devereux, N., Willner, S. P., Ashby, M. L. N., Willmer, C. N. A., & Hriljac, P. 2009, *ApJ*, 702, 955
- Donahue, M., de Messières, G. E., O'Connell, R. W., et al. 2011, *ApJ*, 732, 40
- Doyle, M. T., et al. 2005, *MNRAS*, 361, 34
- Egami, E., Rieke, G. H., Fadda, D., & Hines, D. C. 2006, *ApJ*, 652, L21
- Elbaz, D., Daddi, E., Le Borgne, D., et al. 2007, *A&A*, 468, 33
- Fazio, G. G., et al. 2004, *ApJS*, 154, 10
- Ferland, G. J., Fabian, A. C., Hatch, N. A., et al. 2008, *MNRAS*, 386, L72
- Ferland, G. J., Fabian, A. C., Hatch, N. A., et al. 2009, *MNRAS*, 392, 1475
- Fumagalli, M., Krumholz, M. R., Prochaska, J. X., Gavazzi, G., & Boselli, A. 2009, *ApJ*, 697, 1811
- Gavazzi, G., & Boselli, A. 1996, *Astrophysical Letters Communications*, 35, 1
- Gavazzi, G., Boselli, A., Mayer, L., Iglesias-Paramo, J., Vílchez, J. M., & Carrasco, L. 2001, *ApJ*, 563, L23
- Gavazzi, G., Boselli, A., Donati, A., Franzetti, P., & Scodreggio, M. 2003, *A&A*, 400, 451
- Gavazzi, G., Boselli, A., Cortese, L., Arosio, I., Gallazzi, A., Pedotti, P., & Carrasco, L. 2006, *A&A*, 446, 839
- Guillard, P., Boulanger, F., Pineau des Forêts, G., et al. 2012, *ApJ*, 749, 158
- Guillard, P., Ogle, P. M., Emonts, B. H. C., et al. 2012, *ApJ*, 747, 95
- Georgiev, I. Y., Hilker, M., Puzia, T. H., Chanamé, J., Mieske, S., Goudfrooij, P., Reisenegger, A., & Infante, L. 2006, *A&A*, 452, 141
- Gunn, J. E., & Gott, J. R., III 1972, *ApJ*, 176, 1
- Hollenbach, D., & McKee, C. F. 1989, *ApJ*, 342, 306
- Houck, J. R., et al. 2004, *ApJS*, 154, 18
- Iglesias-Paramo, J., Boselli, A., Cortese, L., Vílchez, J. M., & Gavazzi, G. 2002, *A&A*, 384, 383
- Ikebe, Y., Reiprich, T. H., Böhringer, H., Tanaka, Y., & Kitayama, T. 2002, *A&A*, 383, 773
- Johnstone, R. M., Hatch, N. A., Ferland, G. J., et al. 2007, *MNRAS*, 382, 1246
- Kaufman, M. J., Wolfire, M. G., & Hollenbach, D. J. 2006, *ApJ*, 644, 283
- Kenney, J. D. P., & Koopmann, R. A. 1999, *AJ*, 117, 181
- Kenney, J. D. P., van Gorkom, J. H., & Vollmer, B. 2004, *AJ*, 127, 3361
- Kennicutt, R. C., Jr., & Kent, S. M. 1983, *AJ*, 88, 1094
- Koribalski, B. S., et al. 2004, *AJ*, 128, 16
- Le Petit, F., Nehmé, C., Le Bourlot, J., & Roueff, E. 2006, *ApJS*, 164, 506
- Maloney, P. R., Hollenbach, D. J., & Tielens, A. G. G. M. 1996, *ApJ*, 466, 561
- Mei, S., Blakeslee, J. P., Côté, P., et al. 2007, *ApJ*, 655, 144
- Mohr, J. J., Mathiesen, B., & Evrard, A. E. 1999, *ApJ*, 517, 627
- Ogle, P., Boulanger, F., Guillard, P., et al. 2010, *ApJ*, 724, 1193
- Poggianti, B. M., Smail, I., Dressler, A., et al. 1999, *ApJ*, 518, 576
- Rieke, G. H., Alonso-Herrero, A., Weiner, B. J., et al. 2009, *ApJ*, 692, 556
- Rigopoulou, D., Kunze, D., Lutz, D., Genzel, R., & Moorwood, A. F. M. 2002, *A&A*, 389, 374
- Roediger, E., & Brügger, M. 2008, *MNRAS*, 388, 465
- Roussel, H., et al. 2007, *ApJ*, 669, 959
- Rubin, R. H. 1989, *ApJS*, 69, 897
- Salim, S., et al. 2007, *ApJS*, 173, 267
- Schroeder, A., & Visvanathan, N. 1996, *A&AS*, 118, 441
- Scott, T. C., et al. 2010, *MNRAS*, 403, 1175
- Sivanandam, S., Rieke, M. J., & Rieke, G. H. 2010, *ApJ*, 717, 147
- Smith, B. J., & Madden, S. C. 1997, *AJ*, 114, 138
- Smith, J. D. T., et al. 2007, *PASP*, 119, 1133
- Smith, J. D. T., et al. 2007, *ApJ*, 656, 770
- Smith, R. J., et al. 2010, *MNRAS*, 1238
- Sun, M., Jones, C., Forman, W., Nulsen, P. E. J., Donahue, M., & Voit, G. M. 2006, *ApJ*, 637, L81
- Sun, M., Donahue, M., & Voit, G. M. 2007, *ApJ*, 671, 190
- Sun, M., Donahue, M., Roediger, E., Nulsen, P. E. J., Voit, G. M., Sarazin, C., Forman, W., & Jones, C. 2010, *ApJ*, 708, 946
- Tyler, K. D., Rieke, G. H., & Bai, L. 2013, *ApJ*, 773, 86
- Vollmer, B., Soida, M., Otmianowska-Mazur, K., Kenney, J. D. P., van Gorkom, J. H., & Beck, R. 2006, *A&A*, 453, 883
- Vollmer, B., Braine, J., Pappalardo, C., & Hily-Blant, P. 2008, *A&A*, 491, 455
- Vollmer, B., Wong, O. I., Braine, J., Chung, A., & Kenney, J. D. P. 2012, *A&A*, 543, A33
- White, D. A. 2000, *MNRAS*, 312, 663
- Wong, O. I., Kenney, J. D. P., Murphy, E. J., & Helou, G. 2014, *ApJ*, 783, 109
- Wu, Y., Bernard-Salas, J., Charmandaris, V., et al. 2008, *ApJ*, 673, 193
- Yagi, M., Yoshida, M., Komiyama, Y., et al. 2010, *AJ*, 140, 1814